

ASTRONOMICAL INSTITUTE
SLOVAK ACADEMY OF SCIENCES

CONTRIBUTIONS
OF THE ASTRONOMICAL OBSERVATORY
SKALNATÉ PLESO

• VOLUME LII •

Number 1



April 2022

Editorial Board

Editor-in-Chief

Augustín Skopal, *Tatranská Lomnica, The Slovak Republic*

Managing Editor

Richard Komžík, *Tatranská Lomnica, The Slovak Republic*

Editors

Drahomír Chochol, *Tatranská Lomnica, The Slovak Republic*

Július Koza, *Tatranská Lomnica, The Slovak Republic*

Aleš Kučera, *Tatranská Lomnica, The Slovak Republic*

Luboš Neslušan, *Tatranská Lomnica, The Slovak Republic*

Vladimír Porubčan, *Bratislava, The Slovak Republic*

Theodor Pribulla, *Tatranská Lomnica, The Slovak Republic*

Advisory Board

Bernhard Fleck, *Greenbelt, USA*

Arnold Hanslmeier, *Graz, Austria*

Marian Karlický, *Ondřejov, The Czech Republic*

Tanya Ryabchikova, *Moscow, Russia*

Giovanni B. Valsecchi, *Rome, Italy*

Jan Vondrák, *Prague, The Czech Republic*



Astronomical Institute of the Slovak Academy of Sciences
2022

ISSN: 1336–0337 (on-line version)

CODEN: CAOPF8

Editorial Office: Astronomical Institute of the Slovak Academy of Sciences
SK - 059 60 Tatranská Lomnica, The Slovak Republic

CONTENTS

EDITORIAL

A. Skopal, R. Komžík: Editorial	64
--	----

STARS

Y. Takeda: Photospheric silicon abundances of upper main-sequence stars derived from Si II 6347/6371 doublet lines	5
W.H. Elsanhoury, Amnah S. Al-Johani, Noha H. El Fewaty, A.A. Haroon: Distance determination by magnitude analysis of some open clusters with GAIA <i>era</i> and stellar luminosity function	32
D. Yu. Tsvetkov, I.M. Volkov, S. Yu. Shugarov, V.G. Metlov, N.N. Pavlyuk, O.V. Vozyakova, N.I. Shatsky: Photometric observations of SN 2017egm and peculiar transient AT 2018cow	46

The Contributions of the Astronomical Observatory Skalnaté Pleso
are available in a full version
in the frame of ADS Abstract Service
and can be downloaded in a usual way from the URL address:

<https://ui.adsabs.harvard.edu/>

as well as from the web-site of
the Astronomical Institute of the Slovak Academy of Sciences
on the URL address:

<https://www.astro.sk/caosp/caosp.php>


The journal is covered/indexed by:

Thomson Reuters services (ISI)

Science Citation Index Expanded (also known as SciSearch®)
Journal Citation Reports/Science Edition

SCOPUS

Photospheric silicon abundances of upper main-sequence stars derived from Si II 6347/6371 doublet lines

Yoichi Takeda 

11-2 Enomachi, Naka-ku, Hiroshima-shi, 730-0851, Japan
(E-mail: ytakeda@js2.so-net.ne.jp)

Received: September 24, 2021; Accepted: October 22, 2021

Abstract. Silicon abundances were determined by applying the spectrum-fitting technic to the Si II doublet lines at 6347 and 6371 Å for a sample of 120 main-sequence stars in the T_{eff} range of ~ 7000 – 14000 K (comprising not only normal stars but also non-magnetic chemically peculiar stars) with an aim of investigating their behaviors (e.g., correlation with stellar parameters and abundances of other elements such as Fe or C) and the background physical mechanisms involved therein, where attention was paid to taking into account of the non-LTE effect and to assigning a reasonable value of microturbulence. The following trends were revealed from the analysis: (i) The resulting [Si/H] values, mostly ranging from ~ -0.5 to $\sim +0.3$, show a positive correlation with [Fe/H]. (ii) A kind of anti-correlation exists between Si and C as seen from the tendency of [C/Si] steeply decreasing with [Si/H]. (iii) Si abundances do not show any clear dependence upon T_{eff} or $v_e \sin i$, while Am and HgMn stars appear to show comparatively higher [Si/H] than normal stars. Although it is not straightforward to explain these observational facts, different physical processes (gas–dust separation and atomic diffusion) are likely to be intricately involved in producing these characteristic behaviors of Si composition in the surface of late A through late B dwarfs.

Key words: physical processes: diffusion – stars: abundances – stars: atmospheres – stars: chemically peculiar – stars: early-type

1. Introduction

It is known that a significant fraction of late A through late B-type main sequence stars show anomalous spectra indicative of surface abundance anomalies. Those chemically peculiar (CP) stars are divided into several groups according to their features as summarized in the review paper by Preston (1974). So far, the abundance characteristics of many elements in CP stars have been investigated in comparison with normal stars to discuss the origin of their anomalies.

However, regarding silicon, an important abundant element used as the fiducial reference in geo- or cosmo-chemistry, its abundance behavior in upper main-sequence stars is not yet well understood. While conspicuous overabundance of

Si is known to be observed in magnetic CP stars (CP2; the group 2 in CP stars classified by Preston 1974), how it behaves in non-magnetic CP stars (CP1 — Am stars; CP3 — HgMn stars) or in normal stars is not clear. As a matter of fact, we still do not know whether any Si anomaly ever exists in these stars. According to the atomic diffusion theory (see, e.g., Michaud et al. 2015), which is considered to be a promising mechanism to explain the origin of abundance characteristics in CP stars, Si is expected to be somewhat underabundant (Richer et al. 2000; Talon et al. 2006). Meanwhile, such a trend is not necessarily seen in spectroscopically determined Si abundances of A- and late B-type dwarfs, which are rather diversified around the normal (solar) abundance (somewhat overabundant or underabundant depending on cases; e.g., Niemczura et al. 2015; Ghazaryan, Alecian 2016; Mashonkina et al. 2020b; Saffe et al. 2021), though Si abundance determination significantly depends upon which line is to be used.

Another noteworthy aspect characterizing the importance of Si abundance is that this element is a typical refractory species (being easily fractionated into dust) in contrast to the volatile elements such as C, N, and O. Interestingly, Holweger and Stürenburg (1993) reported that even normal early A-type stars (like λ Boo-type stars) show anti-correlation between the abundances of Si and C ($[\text{C}/\text{Si}]$ systematically decreases with $[\text{Si}/\text{H}]$), which means that some kind of gas–dust separation process (its degree being different from star to star) would have operated in the star formation phase and altered the primordial composition of gas. Is such an effect observed also stars of other types (i.e., late A through late B stars including CP1 and CP3 stars)? This is an interesting problem to be clarified.

Conveniently, Takeda et al. (2018; hereinafter referred to as T18) recently published the C, N, and O abundances for a large sample of 100 main-sequence stars (comprising normal as well as non-magnetic CP stars) covering $7000 \lesssim T_{\text{eff}} \lesssim 11000$ K. It would be worthwhile, therefore, to determine the Si abundances for these stars. This would enable to clarify the behaviors of both $[\text{Si}/\text{H}]$ and $[\text{C}/\text{Si}]$, by which the nature of abundance peculiarity of Si (if any exists) in late A through late B-type stars and the involved physical process may be investigated. This is the aim of the present study.

In the past Si abundance determinations in upper main-sequence stars so far, it appears that neutral Si I lines were mainly used in late–mid A-type stars (including classical Am stars) while once-ionized Si II lines were primarily employed in early A and late B stars (because Si I lines quickly fade out with an increase in T_{eff}). Since the mixed use of lines of different ionization stages is not advantageous because of inevitable line-by-line abundance discrepancies (see, e.g., Mashonkina 2020a), we decided to invoke in this study only the Si II doublet lines at 6347 and 6371 Å, which are of high quality (i.e., almost free from blending) and sufficiently strong over the whole relevant T_{eff} range. Nevertheless, some disadvantages are involved in using these strong Si II lines; that is, the resulting Si abundances suffer an appreciable non-LTE affect and are

sensitive to the microturbulence parameter. Accordingly, special attention had to be paid to these two points.

2. Observational data

Regarding the program stars in this study, all the 101 targets (including the reference star Procyon) in T18 (cf. Section 2 therein) were adopted without change. In addition, in order to back up the range of $11000 \lesssim T_{\text{eff}} \lesssim 14000$ K (which was not covered in T18), 19 late B-type stars (among which $\sim 40\%$ are CP3 stars) were newly included. As such, our targets are 120 late B-type through early F-type stars on or near to the main sequence (luminosity classes of III–V) which have slow to moderately-high rotational velocities ($0 \text{ km s}^{-1} \lesssim v_e \sin i \lesssim 100 \text{ km s}^{-1}$). Among these, about $\sim 1/3$ are non-magnetic CP stars: 25 Am stars, 13 HgMn (or Mn) stars, and 2 λ Boo stars. Besides, our sample includes 16 Hyades A-type stars. The list of these 120 stars is given in Table 1, while the data source and the basic information of the observational materials are summarized in Table 2.

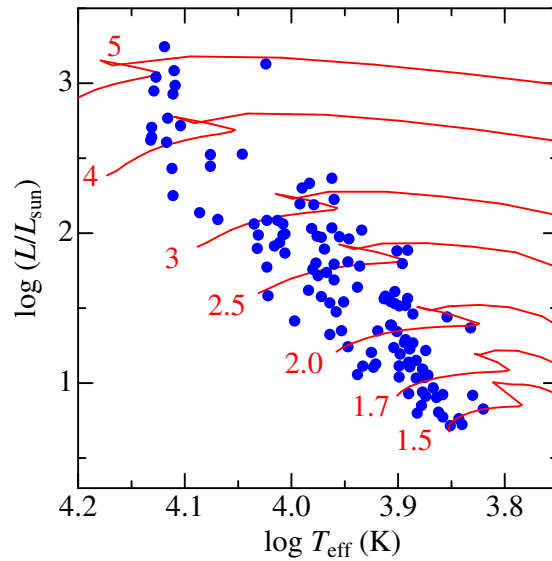


Figure 1. The 120 program stars are plotted on the theoretical HR diagram ($\log(L/L_{\odot})$ vs. $\log T_{\text{eff}}$), where T_{eff} was derived from colors (cf. Section 3) and L was evaluated from visual magnitude (corrected for interstellar extinction by following Arenou et al. 1992), Hipparcos parallax (van Leeuwen 2007), and bolometric correction (Flower 1996). Theoretical solar-metallicity tracks for 7 different masses (1.5, 1.7, 2, 2.5, 3, 4, and $5 M_{\odot}$), which were computed by Lejeune and Schaerer (2001), are also depicted by solid lines for comparison.

Table 1. Stellar parameters and the resulting abundances of the program stars

HD# (1)	Name (2)	Sp.Type (3)	T_{eff} (4)	$\log g$ (5)	[Fe/H] (6)	$v_e \sin i$ (7)	[C/H] (8)	ξ_{std} (9)	[Si/H] $_{\text{std}}$ (10)	ξ_{refit} (11)	[Si/H] $_{\text{refit}}$ (12)	Group (13)	Remark (14)
002628	28 And	A7III	7143	3.48	-0.27	19	-0.32	3.35	-0.27	4.27	-0.29	D	
005448	μ And	A5V	8147	3.82	-0.14	72	-0.32	3.98	-0.31	1.31	+0.22	B	
011529	ω Cas	B8III	12858	3.43	-0.15	30	...	1.00	-0.02	F	SB _o
011636	β Ari	A5V...	8294	4.12	+0.15	73	-0.49	3.93	-0.09	4.01	-0.02	B	SB _o
012111	48 Cas	A3IV	7910	4.08	-0.23	76	-0.46	3.99	-0.27	1.26	+0.25	B	SB _o
012216	50 Cas	A2V	9553	3.90	+0.15	88	-0.20	2.58	-0.29	2.27	-0.17	B	SB2
013161	β Tri	A5III	7957	3.68	-0.32	65	-0.42	4.00	-0.48	B	SB2 _o
014252	10 Tri	A2V	9023	3.64	-0.04	23	-0.53	3.27	-0.32	2.19	-0.08	D	V
016350		B9.5V	9824	3.72	-0.03	21	-0.63	2.22	-0.25	D	
017081	π Cet	B7IV	13063	3.72	-0.10	20	...	1.00	+0.05	2.98	-0.18	F	SB
017093	38 Ari	A7III-IV	7541	3.95	-0.23	69	-0.46	3.81	-0.26	B	V
018454	4 Eri	A5IV/V	7740	4.07	+0.24	100	-0.40	3.94	+0.07	B	V
020149		A1Vs	9522	3.99	-0.05	21	-0.25	2.62	-0.31	2.63	-0.24	D	SB?
020320	ζ Eri	A5m	7505	3.91	-0.12	67	-0.72	3.78	-0.30	2.36	-0.03	B	SB _o , Am
020346		A2IV	8824	3.56	+0.07	21	-0.47	3.50	-0.28	2.98	-0.13	D	SB?
023281		A5m	7761	4.19	+0.05	76	-0.36	3.95	-0.16	3.14	+0.02	B	Am
023408	20 Tau	B8III	12917	3.36	+0.16	30	...	1.00	-0.74	1.39	-0.71	F	SB
023878	τ^7 Eri	A1V	8674	3.80	+0.18	25	-0.63	3.65	-0.17	3.83	-0.12	D	V?
024740	32 Tau	F2IV	6768	3.77	-0.11	21	-0.07	2.71	+0.00	4.58	-0.12	D	V
025490	ν Tau	A1V	9077	3.93	-0.05	82	-0.37	3.20	-0.41	3.19	-0.33	B	
026322	44 Tau	F2IV-V	6795	3.46	-0.15	6	-0.14	2.76	-0.20	2.68	-0.12	D	
027045	ω^2 Tau	A3m	7552	4.26	+0.36	62	-0.89	3.82	+0.10	3.63	+0.20	B	SB, Am

Table 1. Continued.

HD# (1)	Name (2)	Sp.Type (3)	T_{eff} (4)	$\log g$ (5)	[Fe/H] (6)	$v_e \sin i$ (7)	[C/H] (8)	ξ_{std} (9)	[Si/H] $_{\text{std}}$ (10)	ξ_{refit} (11)	[Si/H] $_{\text{refit}}$ (12)	Group (13)	Remark (14)
027628	60 Tau	A3m	7218	4.05	+0.10	30	-1.08	3.45	+0.15	4.26	+0.12	B	SB1o, Am, H
027749	63 Tau	A1m	7448	4.21	+0.41	13	-1.30	3.73	+0.09	4.05	+0.12	B	SB1o, Am, H
027819	δ^2 Tau	A7V	8047	3.95	-0.05	45	-0.15	4.00	-0.17	4.33	-0.14	B	SB, H
027934	κ^1 Tau	A7IV-V	8159	3.84	+0.02	83	-0.17	3.98	-0.21	3.70	-0.10	B	SB?, H
027962	δ^3 Tau	A2IV	8923	3.94	+0.25	11	-0.49	3.39	-0.08	3.08	+0.03	A	SB, H
028226		Am	7361	4.01	+0.31	81	-0.37	3.63	+0.16	B	SB2, Am, H
028319	θ^2 Tau	A7III	7789	3.68	-0.13	68	-0.26	3.96	-0.22	3.28	-0.05	B	SB1o, H
028355	79 Tau	A7V	7809	3.98	+0.19	87	-0.39	3.97	-0.06	2.37	+0.27	B	V?, H
028546	81 Tau	Am	7640	4.17	+0.23	28	-0.44	3.88	-0.05	4.18	-0.01	B	V?, Am, H
029388	90 Tau	A6V	8194	3.88	-0.01	82	-0.18	3.97	-0.13	3.28	+0.05	B	SB1, H
029479	σ^1 Tau	A4m	8406	4.14	+0.35	56	-0.52	3.87	+0.06	4.06	+0.10	B	SBo, Am, H
029499		A5m	7638	4.08	+0.29	61	-0.44	3.88	+0.19	3.98	+0.25	B	V, Am, H
030121	4 Cam	A3m	7700	3.98	+0.27	57	...	3.92	+0.03	3.34	+0.19	B	Am
030210		Am...	7927	3.94	+0.40	56	-1.60	4.00	+0.19	4.46	+0.20	B	SB1?, Am, H
032115		A8IV	7207	4.13	-0.06	10	-0.11	3.44	-0.10	3.90	-0.06	D	V
032537	9 Aur	F0V	6970	4.07	-0.18	20	-0.26	3.07	-0.19	4.64	-0.23	D	SBo
033204		A5m	7530	4.06	+0.18	34	-0.85	3.80	+0.01	3.12	+0.18	B	Am, H
033254	16 Ori	A2m	7747	4.14	+0.28	13	-1.33	3.94	-0.02	3.90	+0.06	B	SBo, Am, H
033641	μ Aur	A4m	7961	4.21	+0.18	79	-0.49	4.00	-0.07	0.82	+0.57	B	V, Am
038899	134 Tau	B9IV	10774	4.02	+0.00	26	...	1.16	-0.05	1.69	-0.05	F	V
039945		A5V	7827	3.36	-0.33	22	-0.34	3.97	-0.52	2.82	-0.31	D	
040626		B9.5IV	10263	4.00	+0.20	14	-0.26	1.69	-0.08	1.12	+0.08	D	

Table 1. Continued.

HD#	Name	Sp.Type	T_{eff}	$\log g$	[Fe/H]	$v_e \sin i$	[C/H]	ξ_{std}	[Si/H] _{std}	ξ_{refit}	[Si/H] _{refit}	Group	Remark
(1)	(2)	(3)	(4)	(5)	(6)	(7)	(8)	(9)	(10)	(11)	(12)	(13)	(14)
040932	μ Ori	Am...	8005	3.93	-0.12	11	-0.64	4.00	-0.35	3.45	-0.22	B	SB1o, Am, H
042035		B9V	10575	3.82	-0.16	2	-0.68	1.35	-0.56	1.09	-0.47	D	V
043378	2 Lyn	A2Vs	9210	4.09	-0.15	46	-0.27	3.03	-0.32	2.99	-0.25	B	V?
045394	16 Gem	A2Vs	8630	3.42	-0.40	23	-0.62	3.69	-0.51	3.16	-0.38	D	
047105	γ Gem	A0IV	9115	3.49	-0.03	11	-0.27	3.16	-0.39	2.58	-0.24	A	SB
048915	α CMa	A0m...	9938	4.31	+0.45	17	-1.09	2.08	+0.06	1.82	+0.17	A	SBo, Am
053244	γ CMa	B8II	13467	3.42	+0.06	36	...	1.00	-0.13	F	V
054834		A9V	7273	4.21	+0.03	30	-0.20	3.53	-0.13	3.32	-0.03	D	
058142	21 Lyn	A1V	9384	3.74	-0.05	19	-0.45	2.81	-0.30	1.36	+0.01	D	V
060179	α Gem	A2Vm	9122	3.88	-0.02	19	-0.93	3.15	-0.23	2.44	-0.05	B	SB1o, Am
061421	α CMi	F5IV-V	6612	4.00	+0.00	9	+0.00	1.97	+0.00	2.67	+0.00	E	SBo
067959		A1V	9168	3.65	+0.07	16	-0.47	3.09	-0.24	2.90	-0.14	D	
072037	2 UMa	A2m	7918	4.16	+0.19	12	-1.53	3.99	-0.18	3.53	-0.06	B	Am
072660		A1V	9635	3.97	+0.37	5	-0.77	2.47	+0.02	2.31	+0.11	D	
074198	γ Cnc	A1IV	9381	4.11	+0.25	85	-0.30	2.81	-0.09	2.45	+0.04	B	SB
075469		A2Vs	9165	3.51	-0.08	22	-0.42	3.09	-0.31	2.49	-0.14	D	
076543	σ^1 Cnc	A5III	8330	4.18	+0.38	91	-0.54	3.91	+0.13	0.50	+0.81	B	SB
077350	ν Cnc	A0III	10141	3.68	+0.24	20	-0.56	1.83	-0.34	C	SBo, Hg
078316	κ Cnc	B8IIIMNp	13513	3.85	+0.33	8	...	1.00	+0.02	C	SB1o, Hg
079158	36 Lyn	B8IIIMNp	13535	3.72	+1.05	46	...	1.00	+0.32	3.25	+0.03	C	V, Hg
079469	θ Hya	B9.5V	10510	4.20	-0.02	82	-0.30	1.42	-0.49	1.19	-0.40	B	SB
084107	15 Leo	A2IV	8665	4.31	+0.01	38	-0.34	3.66	-0.30	3.79	-0.24	B	

Table 1. Continued.

HD# (1)	Name (2)	Sp.Type (3)	T_{eff} (4)	$\log g$ (5)	[Fe/H] (6)	$v_e \sin i$ (7)	[C/H] (8)	ξ_{std} (9)	[Si/H] $_{\text{std}}$ (10)	ξ_{refit} (11)	[Si/H] $_{\text{refit}}$ (12)	Group (13)	Remark (14)
089021	λ UMa	A2IV	8861	3.61	+0.08	52	-0.57	3.46	-0.16	3.18	-0.05	B	V
089822		A0sp...	10307	3.89	+0.47	5	-0.45	1.64	-0.07	1.49	+0.02	C	SB2o, Hg
095382	59 Leo	A5III	8017	3.95	-0.09	68	-0.29	4.00	-0.17	3.71	-0.06	B	
095418	β UMa	A1V	9489	3.85	+0.24	44	-0.63	2.67	-0.10	2.45	+0.01	B	SB
095608	60 Leo	A1m	8972	4.20	+0.31	18	-1.16	3.33	-0.05	3.50	+0.00	B	Am
098664	σ Leo	B9.5Vs	10194	3.75	-0.11	62	-0.29	1.77	-0.33	1.52	-0.22	C	SB
106625	γ Crv	B8III	11902	3.36	-0.51	37	...	1.00	-1.49	1.63	-1.46	C	SB, Hg
116656	ζ UMa	A2V	9317	4.10	+0.28	59	-0.96	2.89	-0.06	2.74	+0.03	B	SB2o
129174	π^1 Boo	B9p MnHg	12929	4.02	-0.06	16	...	1.00	+0.05	0.94	+0.13	C	SB, Hg
130557		B9V $_{\text{svar}}$...	10142	3.85	+0.59	55	-0.55	1.83	-0.24	1.48	-0.11	C	
130841	α^2 Lib	A3IV	8079	3.96	-0.24	58	-1.60	3.99	-0.63	B	SB
140436	γ CrB	A1Vs	9274	3.89	-0.27	68	-1.34	2.95	-0.70	1.61	-0.49	B	
141795	ϵ Ser	A2m	8367	4.24	+0.25	32	-1.01	3.89	-0.11	4.62	-0.12	B	V, Am
143807	ι CrB	A0p...	10828	4.06	+0.35	3	-0.53	1.12	+0.00	0.96	+0.09	D	SB, Hg
144206	ν Her	B9III	11925	3.79	+0.01	12	...	1.00	-0.38	0.57	-0.27	C	Hg
145389	ϕ Her	B9MNP...	11714	4.02	+0.15	11	...	1.00	-0.35	C	SB1o, Hg
149121	28 Her	B9.5III	10748	3.89	+0.24	10	-0.73	1.19	-0.40	0.97	-0.31	C	Hg
150100	16 Dra	B9.5Vn	10542	3.84	-0.33	36	+0.01	1.39	-0.79	C	V
155763	ζ Dra	B6III	13397	4.24	+0.07	41	...	1.00	+0.09	0.88	+0.18	F	V
158716		A1V	9214	4.30	+0.28	4	-0.57	3.03	-0.01	2.79	+0.09	D	
161701		B9V	12692	4.04	+0.85	20	...	1.00	-0.62	C	SB2o, Hg
172167	α Lyr	A0V $_{\text{var}}$	9435	3.99	-0.53	22	-0.21	2.74	-0.65	2.43	-0.54	A	V, LB

Table 1. Continued.

HD#	Name	Sp.Type	T_{eff}	$\log g$	[Fe/H]	$v_e \sin i$	[C/H]	ξ_{std}	[Si/H] _{std}	ξ_{refit}	[Si/H] _{refit}	Group	Remark
(1)	(2)	(3)	(4)	(5)	(6)	(7)	(8)	(9)	(10)	(11)	(12)	(13)	(14)
173648	ζ^1 Lyr	Am	8004	3.90	+0.32	32	-0.69	4.00	+0.01	4.38	+0.03	B	SB1o, Am
173880	111 Her	A5III	8567	4.27	+0.22	72	-0.08	3.75	-0.07	3.57	+0.02	B	SB?
174567		A0Vs	9778	3.59	+0.01	10	-0.40	2.28	-0.28	1.95	-0.16	D	
176984	14 Aql	A1V	9623	3.42	+0.04	29	-0.29	2.49	-0.24	1.24	+0.06	D	V?
179761	21 Aql	B8II-III	12895	3.46	-0.11	16	...	1.00	-0.04	F	V
182564	π Dra	A2III _s	9125	3.80	+0.39	27	-0.35	3.14	-0.03	3.59	-0.03	A	
189849	15 Vul	A4III	7870	3.62	-0.08	11	-0.17	3.99	-0.36	4.09	-0.30	A	SBo
190229		B9MNp...	13102	3.46	+0.72	10	...	1.00	-0.30	C	SB1, Hg
192640	29 Cyg	A2V	8845	3.86	-1.41	74	+0.08	3.48	-1.52	B	V, LB
193432	ν Cap	B9IV	10180	3.91	+0.02	23	-0.27	1.78	-0.12	1.47	+0.01	D	V?
193452		B9.5III/IV	10543	4.15	+0.39	3	-0.86	1.39	-0.09	1.24	-0.01	C	SB1o, Hg
195725	θ Cep	A7III	7816	3.74	+0.16	49	-0.57	3.97	-0.02	4.64	-0.04	B	SB2o
196385		A9V	6919	4.23	-0.21	15	-0.17	2.98	-0.14	4.13	-0.15	D	
196426		B8III _p	12899	3.89	-0.10	6	...	1.00	-0.01	F	
197392		B8II-III	13166	3.46	-0.01	30	...	1.00	-0.06	C	SB
198639	56 Cyg	A4me...	7921	4.09	+0.02	59	-0.38	3.99	-0.23	2.39	+0.08	B	V?, Am
198667	5 Aqr	B9III	11125	3.42	+0.01	26	-0.24	1.00	-0.10	C	V
200499	η Cap	A5V	8081	3.95	-0.17	62	-0.31	3.99	-0.34	4.26	-0.30	B	V
201433		B9V	12193	4.24	+0.00	15	...	1.00	+0.00	C	SBo
202671	30 Cap	B5II/III	13566	3.36	+0.45	25	...	1.00	-0.22	C	V?
204188		A8m	7622	4.21	+0.02	36	-0.43	3.87	-0.18	2.22	+0.13	B	SBo, Am
207098	δ Cap	A5mF2 (IV)	7312	4.06	+0.21	81	-2.00	3.57	+0.02	B	SBo, Am

Table 1. Continued.

HD# (1)	Name (2)	Sp.Type (3)	T_{eff} (4)	$\log g$ (5)	[Fe/H] (6)	$v_e \sin i$ (7)	[C/H] (8)	ξ_{std} (9)	[Si/H] $_{\text{std}}$ (10)	ξ_{refit} (11)	[Si/H] $_{\text{refit}}$ (12)	Group (13)	Remark (14)
209625	32 Aqr	A5m	7700	3.87	+0.24	7	-0.72	3.92	+0.02	4.09	+0.07	D	SB1o, Am
211236		A8/A9IV/V	7488	3.96	-0.21	13	-0.39	3.76	-0.29	4.11	-0.25	D	
212061	γ Aqr	A0V	10384	3.95	-0.08	54	-0.49	1.55	-0.42	2.48	-0.46	B	SB
214994	\circ Peg	A1IV	9453	3.64	+0.18	6	-0.73	2.71	-0.18	2.57	-0.09	A	V
216627	δ Aqr	A3V	8587	3.59	-0.25	79	-0.45	3.73	-0.63	3.87	-0.57	B	V
218396		A5V	7091	4.06	-0.59	41	-0.11	3.27	-0.49	3.54	-0.44	B	
219485		A0V	9577	3.81	-0.05	27	-0.38	2.55	-0.33	1.82	-0.15	D	
222345	ω^1 Aqr	A7IV	7487	3.88	-0.07	86	-0.32	3.76	-0.18	3.11	-0.02	B	SB
222603	λ Psc	A7V	7757	3.99	-0.17	56	-0.27	3.95	-0.25	2.58	+0.02	B	SB
224995	31 Psc	A6V	7779	3.64	-0.13	99	-0.23	3.96	-0.26	D	V

(1) HD number. (2) Bayer/Flamsteed name. (3) Spectral type taken from Hipparcos catalogue (ESA 1997). (4) Effective temperature (in K). (5) Logarithm of surface gravity ($\log g$ in dex, where g is in unit of cm s^{-2}). (6) Fe abundance relative to Procyon. (7) Projected rotational velocity (in km s^{-1}). (8) Non-LTE carbon abundance relative to Procyon determined by Takeda et al. (2018). (9) Standard microturbulent velocity (in km s^{-1}) derived by Equation (1). (10) Non-LTE silicon abundance relative to Procyon corresponding to ξ_{std} . (11) Directly determined microturbulence (in km s^{-1}) as a result of spectrum refitting. (12) Non-LTE silicon abundance relative to Procyon corresponding to ξ_{refit} . (13) Group of the data source (cf. Table 2). (14) Specific remark [spectroscopic binary (SB, “o” denotes the case where orbital elements are available) or radial velocity variable (V), chemical peculiarity type (Am or HgMn or λ Boo), membership of Hyades cluster (H)]. The assigned CP classes were determined by consulting the spectral classifications in three sources: Hipparcos catalogue (ESA 1997), Bright Star Catalogue (Hoffleit, Jaschek 1991), and SIMBAD.

Table 2. Basic information of the observational data.

Group	#Instr.	Obs. Time	Resolution	Number	Star Type	Reference
†A	HIDES	2008 Oct	100000	7	A type	Takeda et al. (2012)
B	BOES	2008 Jan/Sep, 2009 Jan	45000	56	A type	Takeda et al. (2008, 2009)
C	HIDES	2012 May	70000	8	late B type	Takeda et al. (2014)
D	HIDES	2017 Aug/Nov	100000	29	A type	Takeda et al. (2018)
E	HIDES	2001 Feb	70000	1	Procyon	Takeda et al. (2005a)
F	HIDES	2006 Oct	70000	19	late B type	Takeda et al. (2010)

†Only for HD 172167 (Vega), Takeda et al.’s (2007) OAO/HIDES spectrum of high-S/N (~ 2000) and high-resolution (~ 100000) observed in 2006 May was adopted.

#HIDES and BOES denote “High Dispersion Echelle Spectrograph” at Okayama Astrophysical Observatory and “Bohunsan Observatory Echelle Spectrograph” at Bohunsan Optical Astronomy Observatory, respectively.

3. Stellar parameters

As in T18, the effective temperature (T_{eff}) and the surface gravity ($\log g$) for each star were determined from colors of Strömgen’s $uvby\beta$ photometric system by using Napiwotzki et al.’s (1993) calibration.

Especially important parameter we should care about is the microturbulence (ξ). We basically adopted (as done in T18) the analytical T_{eff} -dependent relation derived by Takeda et al. (2008)

$$\xi = 4.0 \exp\{-[\log(T_{\text{eff}}/8000)/A]^2\} \quad (1)$$

(where $A \equiv [\log(10000/8000)]/\sqrt{\ln 2}$, ξ is in km s^{-1} , and T_{eff} is in K) for stars with $T_{\text{eff}} < 11000$ K, while $\xi = 1 \text{ km s}^{-1}$ was assumed at $T_{\text{eff}} > 11000$ K (where this equation yields $\xi < 1 \text{ km s}^{-1}$). Such formula-based values are called as the “standard” microturbulence (designated as ξ_{std}) in order to clarify the difference from another choice of microturbulence described later (cf. Section 6.2).

The only exception is the standard star Procyon (HD 61421),¹ for which we used Takeda et al.’s (2005b) spectroscopically determined values ($T_{\text{eff}} = 6612$ K,

¹ The reason why Procyon was chosen as the reference standard (as done in our previous studies) is to carry out abundance determination by “differential analysis” where the resulting relative abundances are unaffected by uncertainties in the gf values of spectral lines. That is, Procyon (F5 IV–V) is more suitable than the Sun (whose T_{eff} is too low in comparison with those of A and late B stars to be used for such a purpose), while its chemical abundances are

$\log g = 4.00$, and $\xi_{\text{std}} = 1.97 \text{ km s}^{-1}$) to maintain consistency with Takeda et al. (2008).

The adopted values of T_{eff} , $\log g$, $[\text{Fe}/\text{H}]$,² and ξ_{std} are summarized in Table 1. All the program stars are plotted on the $\log L$ vs. $\log T_{\text{eff}}$ diagram (theoretical HR diagram) in Fig. 1, where theoretical evolutionary tracks corresponding to different stellar masses are also depicted. This figure indicates that the masses of our sample stars are in the range between $\sim 1.5M_{\odot}$ and $\sim 5M_{\odot}$. More detailed data regarding the targets and their stellar parameters are given in the electronic table (tableE.dat) available online at

<https://www.astro.sk/caosp/Eedition/FullTexts/vol152no1/pp5-31.dat/>.

The model atmosphere corresponding to each star was constructed by interpolating Kurucz's (1993a) ATLAS9 model grid (for $\xi = 2 \text{ km s}^{-1}$) in terms of T_{eff} , $\log g$, and $[\text{Fe}/\text{H}]$.

4. Non-LTE calculation for Si

The statistical-equilibrium calculations for silicon atom were carried out by using the non-LTE code described in Takeda (1991). The atomic model of Si adopted in this study was constructed based on Kurucz and Bell's (1995) compilation of atomic data (gf values, levels, etc.), which consists of 34 Si I terms (up to $4d^1F^{\circ}$ at 58893.4 cm^{-1}) with 222 Si I radiative transitions, 31 Si II terms (up to $3p^3^4S^{\circ}$ at 123033.5 cm^{-1}) with 109 Si II radiative transitions, and 23 Si III terms (up to $4p^3P$ at 248073 cm^{-1} ; included only for conservation of total Si atoms).

Regarding evaluations of photoionization rates, the cross-section data taken from TOPbase (Cunto, Mendoza 1992) were used for the lower 10 Si I terms and 10 Si II terms (while hydrogenic approximation was assumed for higher terms). As to the collisional rates, the theoretical results of Aggarwal and Keenan (2014) were invoked for the bound-bound electron impact rates between the lower 10 Si II terms. Otherwise, the recipe described in Sect. 3.1.3 of Takeda (1991) was followed (inelastic collisions due to neutral hydrogen atoms were formally included as described therein, though insignificant in the atmosphere of early-type stars under question).

The calculations were done on a grid of 44 ($= 11 \times 4$) solar-metallicity ($[\text{Fe}/\text{H}] = 0$) model atmospheres resulting from combinations of eleven T_{eff} values (6500, 7000, 7500, 8000, 8500, 9000, 9500, 10000, 11000, 12000, 13000, and 14000 K) and four $\log g$ values (3.0, 3.5, 4.0, and 4.5) while assuming $\xi = 2 \text{ km s}^{-1}$ and the Si abundance of $A(\text{Si}) = 7.55$ (solar Si abundance adopted in ATLAS9 models).

practically the same as those of the Sun (cf. the references quoted in Section IV(c) of Takeda et al. 2008).

² These Fe abundances were already established in our previous papers (cf. the references given in Table 2) based on the spectrum-fitting method in the wavelength region ($\sim 20\text{--}30\text{\AA}$ wide) centered around $\sim 6155\text{\AA}$ (where the Fe II 6147/6149 doublet lines are the important indicators of Fe abundance).

The depth-dependent non-LTE departure coefficients to be used for each star were then evaluated by interpolating this grid in terms of T_{eff} and $\log g$.

5. Abundance determination

The non-LTE Si abundances were determined (as done in T18 for CNO abundances) based on Takeda’s (1995) numerical algorithm by accomplishing the best fit between the synthetic and observed spectra in the 6340–6380 Å region while varying the abundances of Si and some other elements showing appreciable lines (especially Fe, plus other elements such as Mg, Mn, Zn depending on cases), v_M (macrobrodening velocity corresponding to instrumental/rotational broadening and macroturbulence) and $\Delta\lambda$ (radial velocity or wavelength shift) but the microturbulence being fixed at ξ_{std} . Since the relevant wavelength region of the raw spectra is more or less contaminated by weak telluric lines, they were removed in advance by dividing by the spectrum of a rapid rotator as demonstrated in Fig. 2. The atomic data of spectral lines comprising in this region were exclusively taken from Kurucz and Bell’s (1995) compilation (those of relevant Si II doublet lines are summarized in Table 3), though some pre-adjustments³ were necessary in order to achieve an satisfactory fit. The accomplished fit in the neighborhood of both lines for each star is displayed in Fig. 3.

Table 3. Adopted atomic data of Si II 6347 and 6371 lines.

Multiplet No.	λ (Å)	χ_{low} (eV)	$\log gf$ (dex)	Gammar (dex)	Gammas (dex)	Gammaw (dex)
2	6347.109	8.121	+0.297	9.09	−5.04	(−7.68)
2	6371.371	8.121	−0.003	9.08	−5.04	(−7.68)

Note.

These data are were taken from Kurucz and Bell’s (1995) compilation, while those parenthesized are the default values calculated by Kurucz’s (1993a) WIDTH9 program.

Followed by first four self-explanatory columns, damping parameters are given in the last three columns:

Gammar is the radiation damping width (s^{-1}), $\log \gamma_{\text{rad}}$.

Gammas is the Stark damping width (s^{-1}) per electron density (cm^{-3}) at 10^4 K, $\log(\gamma_e/N_e)$.

Gammaw is the van der Waals damping width (s^{-1}) per hydrogen density (cm^{-3}) at 10^4 K, $\log(\gamma_w/N_H)$.

³ Six lines (Ca I 6343.308, Si I 6353.360, Fe I 6353.835, Si I 6356.321, Ca I 6361.786, and Fe I 6368.620) included in this database were neglected, while the $\log gf$ of Fe I 6358.631 was changed from -1.04 to -1.70 .

Then, the equivalent widths (W_{6347} and W_{6371}) of the Si II 6347 and 6371 lines were inversely evaluated from the best-fit solution of $A_{\text{std}}^{\text{N}}(\text{Si})$ with the same model and atmospheric parameters as used in the spectrum-fitting analysis. From such evaluated W , the non-LTE abundance (A^{N}), LTE abundance (A^{L}) and non-LTE correction ($\Delta \equiv A^{\text{N}} - A^{\text{L}}$) were derived for each line. Besides, W can be further used to estimate the abundance uncertainties due to typical ambiguities of atmospheric parameters by perturbing the standard values interchangeably. Such derived W_{6347}/W_{6371} (equivalent widths), $\Delta_{6347}/\Delta_{6371}$ (equivalent widths), $A_{\text{std}}^{\text{N}}$ (non-LTE Si abundance), $\delta_{T_{\text{eff}}}$ (abundance changes for T_{eff} perturbations by $\pm 3\%$), $\delta_{g_{\pm}}$ (abundance changes for $\log g$ perturbations by ± 0.1 dex), and $\delta_{\xi_{\pm}}$ (abundance changes for ξ perturbations by $\pm 30\%$) are plotted against T_{eff} in Fig. 4.

These standard abundances, expressed in the form of $[\text{Si}/\text{H}]_{\text{std}} (\equiv A_{\text{std}}^{\text{N}}(\text{star}) - A_{\text{std}}^{\text{N}}(\text{Procyon}))$ are given in Table 1. More complete results including W and Δ are presented in “tableE.dat” of the online material.

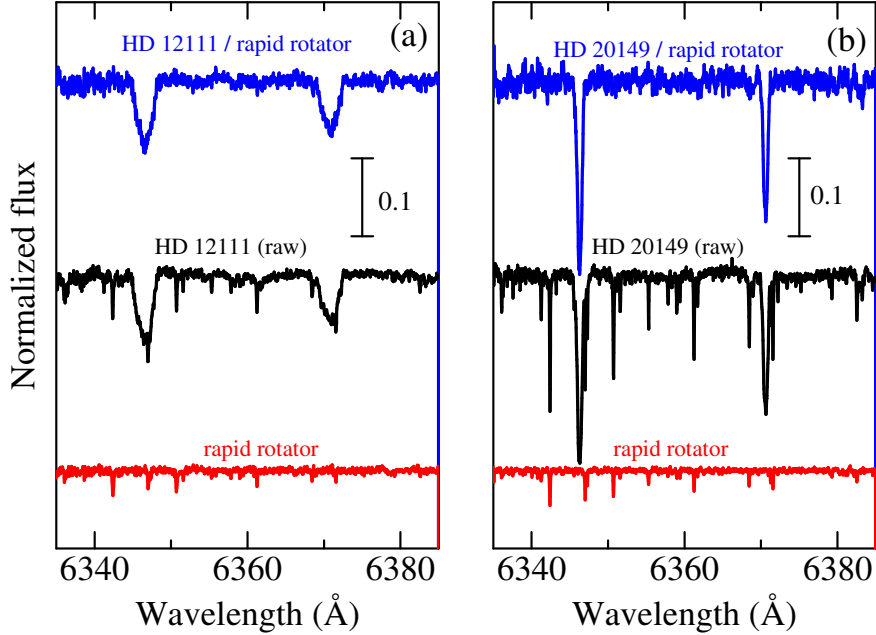


Figure 2. Examples of how the telluric lines (mostly due to H_2O vapor) are removed in the 6340–6380 Å region comprising Si II 6347/6371 lines. Dividing the raw stellar spectrum (middle, black) by the spectrum of a rapid rotator (bottom, red) results in the final spectrum (top, blue). The left (a) and right (b) panel show the cases of HD 12111 (weaker telluric contamination) and HD 20149 (stronger contamination), respectively. No Doppler correction is applied to the wavelength scale of these spectra.

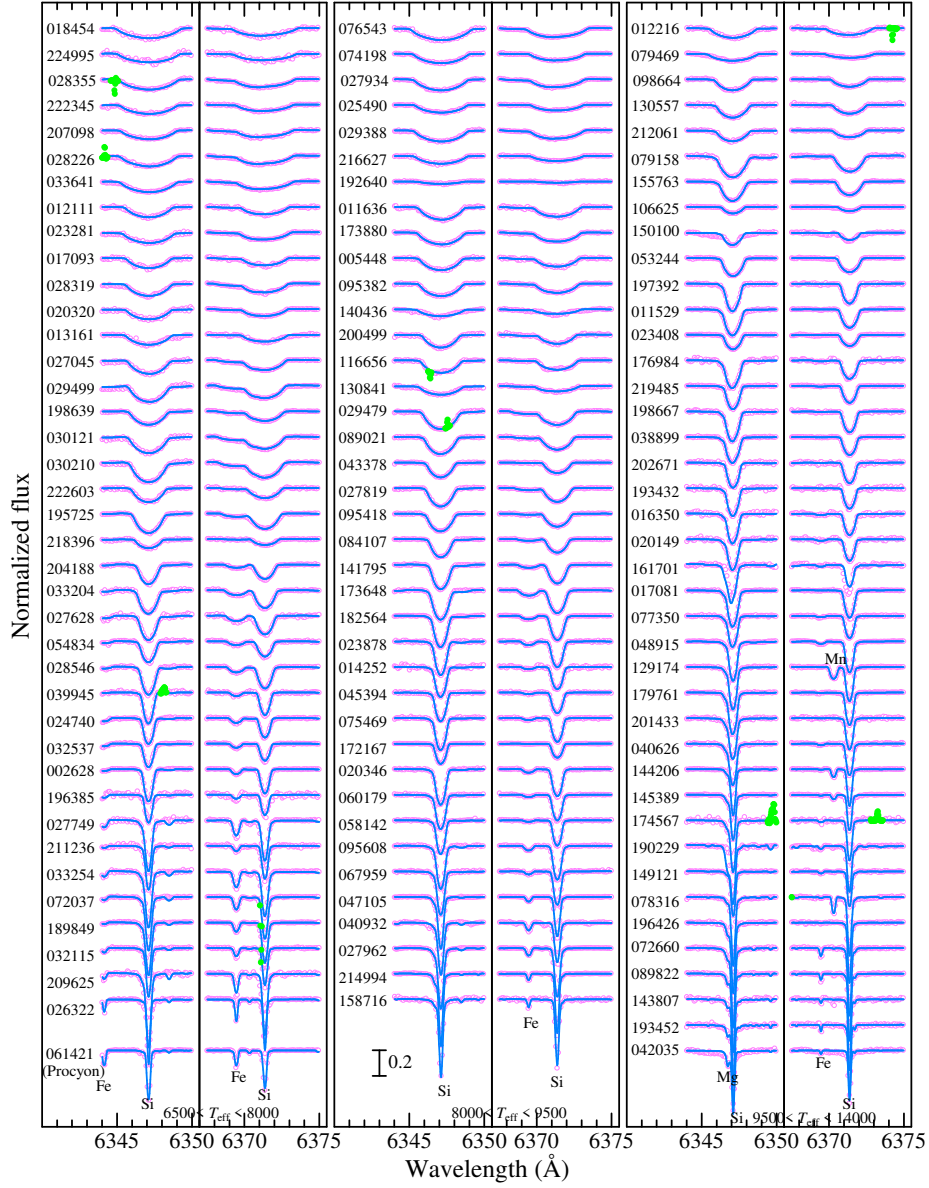


Figure 3. Synthetic spectrum fitting analysis for Si abundance determination from Si II 6347/6371 lines. In the left, middle, and right panels are shown the results for 40 stars in $6500 \text{ K} < T_{\text{eff}} < 8000 \text{ K}$, 39 stars in $8000 \text{ K} < T_{\text{eff}} < 9500 \text{ K}$, and 41 stars in $9500 \text{ K} < T_{\text{eff}} < 14000 \text{ K}$, respectively. The best-fit theoretical spectra (in the selected ranges of $6344\text{--}6350 \text{ \AA}$ and $6367.5\text{--}6375 \text{ \AA}$ comprising the relevant Si II lines) are depicted by blue solid lines, while the observed data are plotted by pink symbols (the masked data excluded in judging the goodness of fit are highlighted in green). In each panel, the spectra are arranged in the descending order of $v_e \sin i$, and an offset of 0.2 is applied to each spectrum (indicated by the HD number) relative to the adjacent one. The case of Procyon (standard star) is separately displayed at the bottom of the left panel.

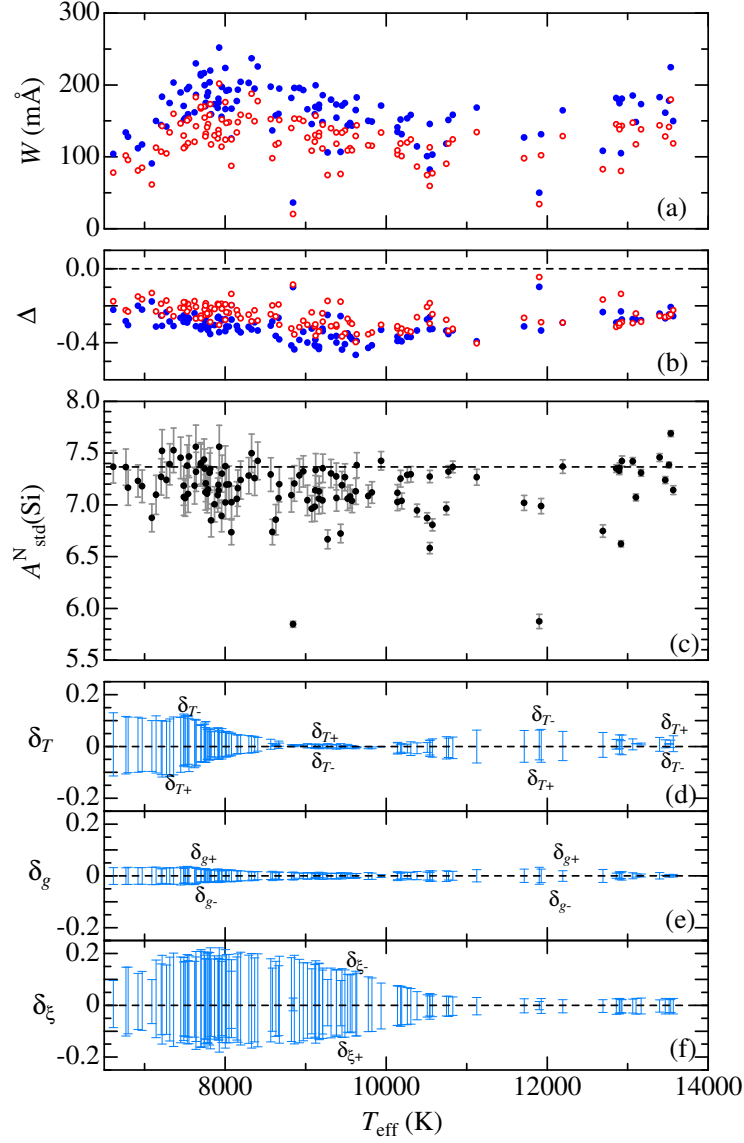


Figure 4. Silicon abundances and the related quantities plotted against T_{eff} . (a) Equivalent widths of Si II 6347 (W_{6347} , filled symbols) and Si II 6371 (W_{6371} , open symbols). (b) Non-LTE corrections for Si II 6347 (Δ_{6347} , filled symbols) and Si II 6371 (Δ_{6371} , open symbols) (c) $A_{\text{std}}^N(\text{Si})$ (standard non-LTE Si abundance corresponding to ξ_{std}), where the error bar denotes $\pm\delta_{T_{gv}}$ (root-sum-square of δ_T , δ_g , and δ_ξ , where δ_T is the mean of $|\delta_{T+}|$ and $|\delta_{T-}|$; etc.), (d) δ_{T+} and δ_{T-} (abundance variations for Si II 6347 in response to T_{eff} changes of +3% and -3%), (e) δ_{g+} and δ_{g-} (abundance variations for Si II 6347 in response to $\log g$ changes by +0.1 dex and -0.1 dex), and (f) $\delta_{\xi+}$ and $\delta_{\xi-}$ (abundance variations for Si II 6347 in response to perturbing the ξ_{std} value by +30% and -30%). The abundance of Procyon ($A_{\text{std}}^N = 7.367$), which is adopted as the reference, is indicated by the horizontal dashed line in panel (c).

6. Discussion and conclusion

6.1. Characteristics of the non-LTE effect

As seen from the results derived in Section 5, the Si II 6347/6371 lines suffer an appreciable non-LTE effect. According to Fig. 4b, their non-LTE abundance corrections (Δ) are negative (which means that the non-LTE effect strengthens the lines) and typically a few tenths dex ($|\Delta_{6347}| \sim 0.2\text{--}0.5$ dex, $|\Delta_{6371}| \sim 0.1\text{--}0.4$ dex; naturally the former is larger because of the stronger line forming in comparatively shallower layer). The maximum of $|\Delta|$ is around $T_{\text{eff}} \sim 10000$ K.

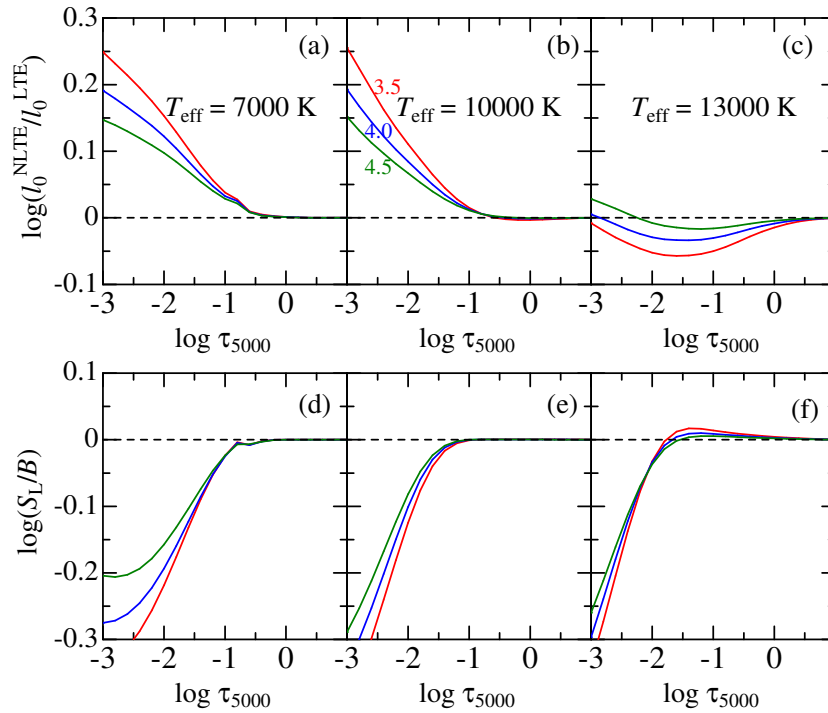


Figure 5. The non-LTE-to-LTE line-center opacity ratio (upper panels a–c) and the ratio of the line source function (S_L) to the local Planck function (B) (lower panels d–f) for the Si II $4s^2S\text{--}4p^2P^o$ transition (corresponding to Si II 6347/6371 lines) of multiplet 2, plotted against the continuum optical depth at 5000 Å. Computations were done with $\xi = 2$ km s $^{-1}$ on the solar-metallicity models ($[\text{Fe}/\text{H}] = [\text{Si}/\text{Fe}] = 0$) of $T_{\text{eff}} = 7000$ K (left panels a, d), 10000 K (middle panels b, e), and 13000 K (right panels c, f). At each panel are shown the results for three $\log g$ values of 3.5, 4.0, and 4.5 depicted by different colors (red, blue, and green, respectively).

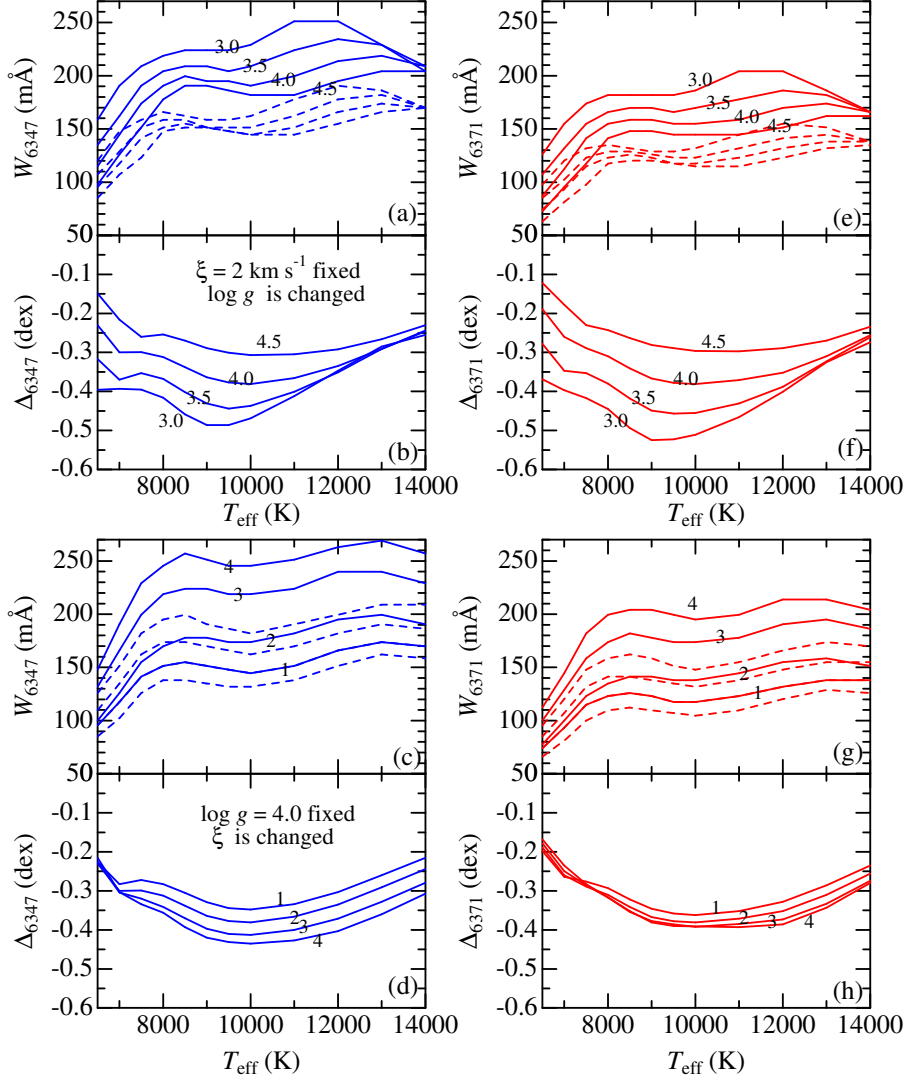


Figure 6. The non-LTE and LTE equivalent widths (W^N and W^L) for the Si II 6347/6371 lines and the corresponding non-LTE corrections (Δ), which were computed on the non-LTE grid of models described in Section 4, are plotted against T_{eff} . Each figure set consists of two panels; the upper panel is for W^N (solid lines) and W^L (dashed lines), while the lower panel is for Δ . The upper sets (a+b, e+f) show the case of fixed ξ (2 km s^{-1}) but different $\log g$ (3.0, 3.5, 4.0, and 4.5), while the lower sets (c+d, g+h) are for the case of fixed $\log g$ (4.0) but different ξ (1, 2, 3, and 4 km s^{-1}). The left-hand figures show the results for the Si II 6347 line, while the right-hand ones for the Si II 6371 line.

In Fig. 5 are shown the $l_0^{\text{NLTE}}(\tau)/l_0^{\text{LTE}}(\tau)$ (the non-LTE-to-LTE line-center opacity ratio; almost equal to $\simeq b_1$) and $S_L(\tau)/B(\tau)$ (the ratio of the line source function to the Planck function; nearly equal to $\simeq b_2/b_1$) for the transition relevant to the Si II 6347/6371 lines (b_1 and b_2 are the non-LTE departure coefficients for the lower and upper terms), which were computed on the models of representative T_{eff} and $\log g$ values. As seen from this figure, while $l_0^{\text{NLTE}}/l_0^{\text{LTE}} > 1$ (overpopulation) holds in the line-forming region at $T_{\text{eff}} \lesssim 10000$ K (A-type stars), this inequality suddenly turns to be reversed (underpopulation) at higher T_{eff} (late B-type stars) because of the beginning of Si II overionization (once-ionized Si is not the dominant ionization stage any more in such a higher T_{eff} regime). Although the non-LTE effect still acts to intensify lines (Δ remains negative) at $10000 \text{ K} \lesssim T_{\text{eff}} \lesssim 14000 \text{ K}$ due to the dilution of $S_L(< B)$ (see the lower panels in Fig. 5), $|\Delta|$ progressively decreases with an increase in T_{eff} (see also the Appendix A where the behavior of Δ in B-type stars is further discussed).

How the theoretical W and Δ computed for these two Si II lines depend upon the atmospheric parameters (T_{eff} , $\log g$, and ξ) is illustrated in Fig. 6, which reasonably explains the trends observed in Figs. 4a and 4b (the maximum of W is seen around $T_{\text{eff}} \sim 8000$ K because the peak of ξ is attained there).

6.2. Consistency check of microturbulence

As is evident from the lower three panels (d–f) of Fig. 4, an uncertainty ξ has the most significant impact on the Si abundance among the three atmospheric parameters especially at $T_{\text{eff}} \lesssim 10000$ K, since the Si II 6347/6371 lines are strong and saturated (on the flat part of the curve of growth). Therefore, particular attention should be paid to whether or not an appropriate choice of ξ has been done. As a matter of fact, Takeda et al. (2009) reported that considerably underestimated Na abundance would result from the strongly saturated Na I 5889/5895 D lines if the microturbulence given by Equation (1) is used, which may be attributed to the depth-dependence of ξ (cf. Section 5 therein) Does such an inadequacy similarly exist also for the case of Si II 6347/6371 lines?

In order to examine this problem, another solution of microturbulence was determined from these doublet lines themselves by taking the advantage that their $\log gf$ strengths are different by 0.3 dex. That is, spectrum fitting analysis was retried (taking $A_{\text{std}}^{\text{N}}$ and ξ_{std} as the starting solutions) while allowing *both* $A^{\text{N}}(\text{Si})$ and ξ to vary. These refit solutions (which are referred to as $A_{\text{refit}}^{\text{N}}$ and ξ_{refit}) were successfully converged for 97 stars (about $\sim 80\%$), though failed for the remaining 23 stars.

The resulting $A_{\text{refit}}^{\text{N}}$ and ξ_{refit} (given in Table 1) are compared with $A_{\text{std}}^{\text{N}}$ and ξ_{std} in Fig. 7, where the following characteristics are observed.

— Fig. 7a indicates that consistency between ξ_{refit} (dots) and ξ_{std} (solid line) is not necessarily bad, though considerable discrepancy (quite a few ξ_{refit} values

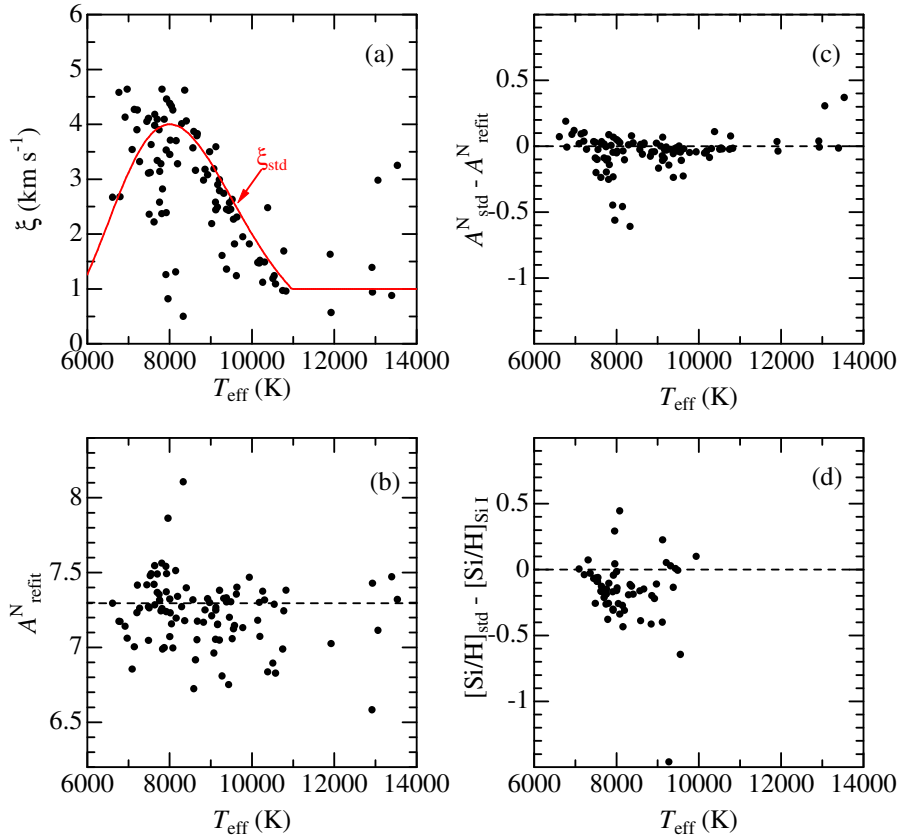


Figure 7. (a) Microturbulence directly determined by spectrum refitting (ξ_{refit}) plotted against T_{eff} by dots, while the T_{eff} -dependent standard microturbulence (ξ_{std}) given by Equation (1) is shown by the red solid line. (b) Non-LTE Si abundance ($A_{\text{refit}}^{\text{N}}$) resulting from refitting (corresponding to ξ_{refit}) plotted against T_{eff} . (c) Difference between “std” and “refit” abundances ($A_{\text{std}}^{\text{N}} - A_{\text{refit}}^{\text{N}}$) plotted against T_{eff} . (d) Difference between $[\text{Si}/\text{H}]_{\text{std}}$ (derived in this study based on Si II 6347/6371 lines by using the standard ξ_{std}) and $[\text{Si}/\text{H}]_{\text{Si I}}$ (derived by Takeda et al. 2009) based on the spectrum fitting applied to the region comprising Si I lines) plotted against T_{eff} .

tending to be appreciably lower than ξ_{std}) is seen around $T_{\text{eff}} \sim 8000$ K.⁴

— As a result, $A_{\text{std}}^{\text{N}}$ tends to be lower than $A_{\text{refit}}^{\text{N}}$ at $T_{\text{eff}} \sim 8000$ K. The differences are typically a few tenths dex (four stars show especially large discrepancies of

⁴ Besides, two ξ_{refit} values around $T_{\text{eff}} \sim 13000$ K are apparently two large; but they are not reliable and should not be seriously taken, because determination becomes more difficult for the case of weaker Si II lines at higher T_{eff} .

$\sim 0.5\text{--}0.6$ dex (cf. Fig. 7c).

— It is worth noting that the $[\text{Si}/\text{H}]_{\text{std}}^{\text{N}}$ values also exhibit similar discrepancies when compared with Takeda et al.’s (2009) $[\text{Si}/\text{H}]$ results derived from the spectrum fitting in the 6140–6170 Å region comprising Si I lines (Fig. 7d).

— Accordingly, we may state that the abundances derived from Si II 6347/6371 lines by using Equation (1)-based ξ_{std} are apt to be underestimated around $T_{\text{eff}} \sim 8000$ K corresponding to late-to-mid A-type stars.

— However, this problem is not so serious as the case of Na I 5889/5895 lines addressed by Takeda et al. (2009). Actually, the appearance of $A_{\text{refit}}^{\text{N}}$ vs. T_{eff} plot (Fig. 7b) is not significantly different from the case of $A_{\text{std}}^{\text{N}}$ (Fig. 4c). In the figures illustrating the behaviors of Si abundances to be discussed in the next section, both (“std” and “refit”) results will be shown, so that they may be compared with each other.

6.3. Observed trend of Si abundances

The relative abundances of Si ($[\text{Si}/\text{H}]$) and the C-to-Si ratios ($[\text{C}/\text{Si}] = [\text{C}/\text{H}] - [\text{Si}/\text{H}]$) for the 120 stars are plotted against the stellar parameters (and the corresponding $[\text{C}/\text{H}]$ or $[\text{Si}/\text{H}]$) in Fig. 8, where two kinds of results based on $A_{\text{std}}^{\text{N}}$ and $A_{\text{refit}}^{\text{N}}$ are presented in parallel in each panel. Besides, the same correlation plots as Fig. 8 but only for the selected 16 Hyades stars are depicted in Fig. 9. The following characteristics can be read from these figures.

- The resulting Si abundances (relative to Procyon) for most stars are in the range of $-0.5 \lesssim [\text{Si}/\text{H}] \lesssim +0.3$ (tending to be rather Si-deficient than Si-rich).
- As for the relation to stellar parameters, any clear dependence upon T_{eff} or $v_e \sin i$ is not observed in $[\text{Si}/\text{H}]$ (Figs. 9a and 9b).
- Am stars and HgMn stars appear to show somewhat higher $[\text{Si}/\text{H}]$ than normal stars, while λ Boo stars are naturally Si-deficient. The mean $[\text{Si}/\text{H}]_{\text{std}}$ values for each star group are -0.23 (normal), -0.03 (Am), -0.18 (HgMn),⁵ and -1.08 (λ Boo).
- A positive correlation exists between $[\text{Si}/\text{H}]$ and $[\text{Fe}/\text{H}]$ (Fig. 8c), which is also observed for the selected sample of Hyades stars (Fig. 9c). Actually, the correlation coefficients calculated between $[\text{Si}/\text{H}]_{\text{std}}$ and $[\text{Fe}/\text{H}]$ are $+0.65$ (all sample) and $+0.82$ (Hyades sample).
- The C-to-Si ratio ($[\text{C}/\text{Si}]$) tends to decrease systematically with an increase in $[\text{Si}/\text{H}]$ (Fig. 8h) indicating that C and Si are anti-correlated, though the nature of anti-correlation between $[\text{Si}/\text{H}]$ and $[\text{C}/\text{H}]$ is not very clear (Fig. 8d).

⁵ HD 106625 (γ Crv) was excluded in the averaging process because of its exceptionally low $[\text{Si}/\text{H}]_{\text{std}}$ of -1.49 for this HgMn group.

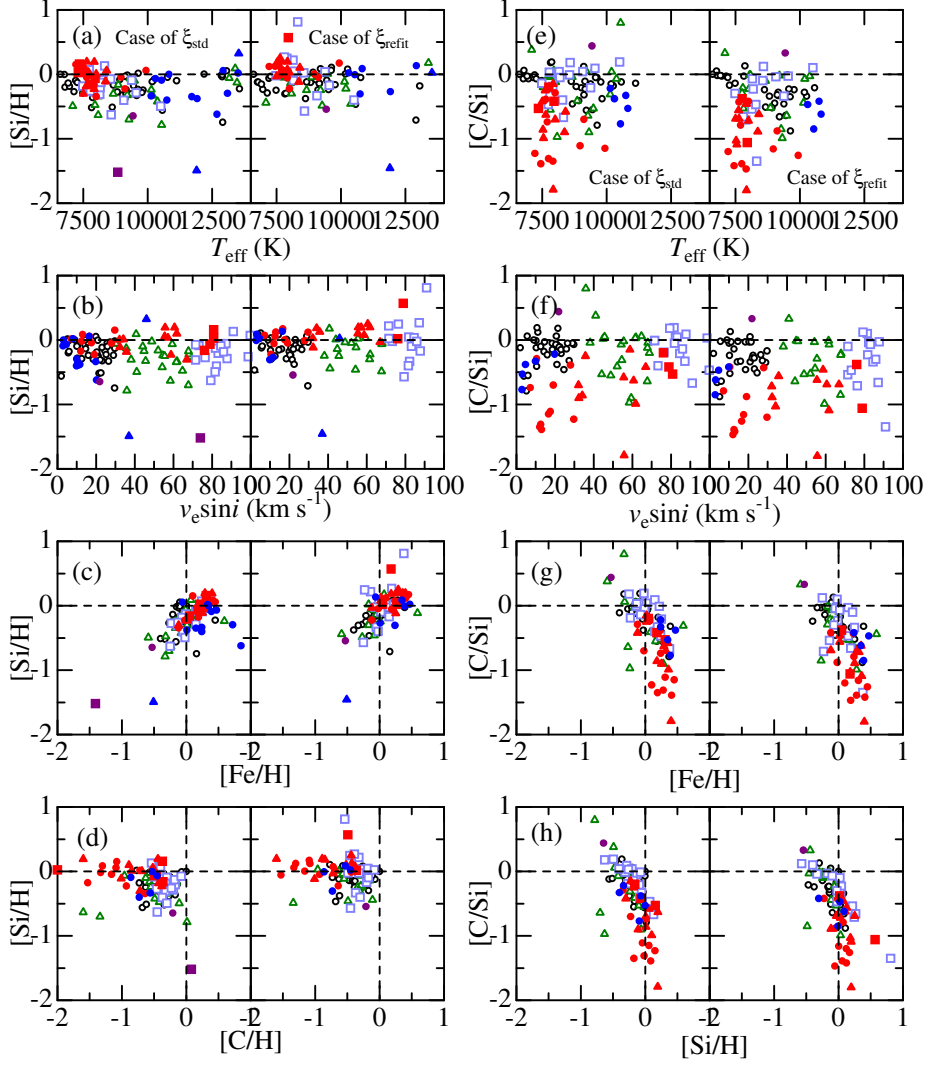


Figure 8. Graphical display of how $[\text{Si}/\text{H}]$ and $[\text{C}/\text{Si}]$ for the 120 program stars are related to stellar parameters (or abundances). Left panels: $[\text{Si}/\text{H}]$ (Si abundance relative to Procyon) plotted against (a) T_{eff} , (b) $v_e \sin i$, (c) $[\text{Fe}/\text{H}]$, and (d) $[\text{C}/\text{H}]$. Right panels: $[\text{C}/\text{Si}]$ (logarithmic C-to-Si abundance ratio) plotted against (e) T_{eff} , (f) $v_e \sin i$, (g) $[\text{Fe}/\text{H}]$, and (h) $[\text{Si}/\text{H}]$. Each panel consists of two similar diagrams constructed from different Si abundances $A_{\text{std}}^{\text{N}}$ (left) and $A_{\text{refit}}^{\text{N}}$ (right) corresponding to ξ_{std} and ξ_{refit} , respectively. Stars of different $v_e \sin i$ classes are discriminated by the types of symbols: circles ($0 < v_e \sin i < 30 \text{ km s}^{-1}$), triangles ($30 \leq v_e \sin i < 70 \text{ km s}^{-1}$), and squares ($70 \leq v_e \sin i < 100 \text{ km s}^{-1}$). Normal stars are shown by open symbols, while those classified as chemically peculiar are highlighted by filled symbols (red-filled symbols for Am stars, blue-filled ones for HgMn stars, and purple-filled ones for λ Boo stars).

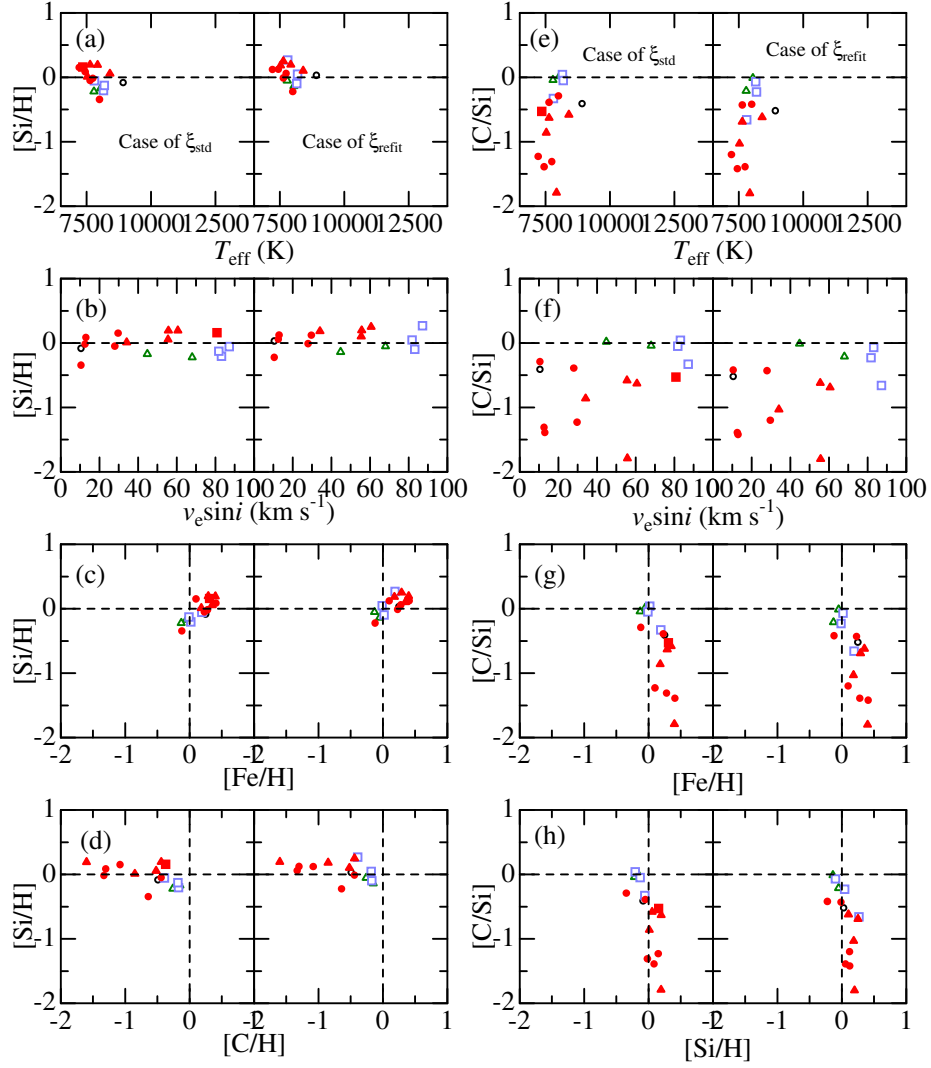


Figure 9. Graphical display of how [Si/H] and [C/Si] for the 16 Hyades cluster stars are related to stellar parameters (or abundances). Otherwise, the same as in Fig. 8.

How can we interpret these results? As mentioned in Section 1, two physical processes may be considered for the possible cause of chemical abundance anomalies: (i) atomic diffusion and (ii) gas–dust separation. Regarding the former diffusion process, although considerable uncertainties still exist, available theoretical calculations predict a deficiency of C, a slight underabundance of Si, and an overabundance of Fe (cf. Richer et al. 2000; Talon et al. 2006). As to the latter gas–dust separation process, Si as well as Fe (both are refractory elements and should behave similarly) are expected to be anti-correlated with C (volatile species).

Although $[C/Si]$ apparently decreases with an increase in $[Si/H]$, this trend can not be simply explained by the gas–dust separation alone, because the (negative) gradient of $d[C/Si]/d[Si/H]$ in Fig. 8h is too steep to be identified with Holweber and Stürenburg’s (1993) Fig. 2 (the slope is $\sim -45^\circ$). Actually, the considerably wide range of $[C/Si]$ (~ 2 dex) is mainly due to the diversified deficiency of C ($-1.5 \lesssim [C/H] \lesssim 0$ especially seen in Am stars of lower T_{eff} ; cf. Fig. 8d) while the contribution of $[Si/H]$ is comparatively minor. Therefore, the main cause of C deficiency is attributed to (not the dust–gas separation but) to atomic diffusion as discussed in T18.

Regarding the cause for the dispersion of $[Si/H]$, the fact that $[Si/H]$ and $[Fe/H]$ correlate well with each other (Fig. 8c, Fig. 9c; just like Holweber and Stürenburg’s Fig. 3) may indicate that the gas–dust separation process (acting both Si and Fe in a same direction) is involved at least partly, because atomic diffusion would differently affect Si and Fe according to the currently available calculations. However, it is unlikely that the diffusion process does not play any role in affecting the surface abundances of Si and Fe, since Takeda and Sadakane (1997) reported the $v_e \sin i$ -dependence of over-/under-abundance of Fe/O in Hyades A-type stars (cf. Fig. 7 therein) which is reasonably interpreted as the result of atomic diffusion being more effective for slower rotators.

Consequently, given the available information alone, it is hardly possible to find any satisfactory interpretation regarding the observed behavior of Si abundances (particularly in relation to the abundances of C and Fe). It may be possible that both processes (atomic diffusion and gas–dust separation) concurrently operate in an intricate manner (the former being more significant?). Unfortunately, the current diffusion calculations appear to still suffer considerable uncertainties (e.g., in the choice of parameters concerning turbulent mixing or mass loss).⁶ Further progress in this field is desirably awaited, so that it may shed light to this complicated situation.

Acknowledgements. This research has made use of the SIMBAD database, operated at CDS, Strasbourg, France.

⁶ In this context, Takeda et al. (2012) pointed out that $[Na/H]$ well correlate with $[Fe/H]$ in A-type stars, which contradicts the prediction from the diffusion theory (Na is expected to be almost normal or slightly underabundant unlike Fe). That situation is quite similar to the present case of $[Si/H]$.

References

- Aggarwal K. M., Keenan F. P., 2014, *MNRAS*, 442, 388 (DOI: 10.1093/mnras/stu883)
- Arenou F., Grenon M., Gómez A., 1992, *A&A*, 258, 104
- Cunto W., Mendoza C., 1992, *Rev. Mex. Astron. Astrofis.*, 23, 107
- ESA, 1997, *The Hipparcos and Tycho Catalogues*, ESA SP-1200, available from NASA-ADC or CDS in a machine-readable form (file name: `hip_main.dat`)
- Flower P. J., 1996, *ApJ*, 469, 355 (DOI: 10.1086/177785)
- Ghazaryan S., Alecian G., 2016, *MNRAS*, 460, 1912 (DOI: 10.1093/mnras/stw911)
- Hoffleit D., Jaschek C., 1991, *The Bright Star Catalogue*, 5th revised edition (New Haven, Conn.: Yale University Observatory)
- Holweger H., Stürenburg S., 1993, in *Peculiar Versus Normal Phenomena in A-Type and Related Stars*, ASP Conf. Ser. 44, eds. M. M. Dworetzky, F. Castelli, and R. Faraggiana (Astronomical Society of the Pacific: San Francisco), p. 356
- Kurucz R. L., 1993a, Kurucz CD-ROM, No. 13 (Harvard-Smithsonian Center for Astrophysics)
- Kurucz R. L., 1993b, Kurucz CD-ROM, No. 14 (Harvard-Smithsonian Center for Astrophysics)
- Kurucz R. L., Bell B., 1995, Kurucz CD-ROM, No. 23 (Harvard-Smithsonian Center for Astrophysics)
- Lejeune T., Schaerer D., 2001, *A&A*, 366, 538 (DOI: 10.1051/0004-6361:20000214)
- Mashonkina L., 2020a, *MNRAS*, 493, 6095 (DOI: 10.1093/mnras/staa653)
- Mashonkina L., Ryabchikova T., Alexeeva S., Sitnova T., Zatsarinny, O., 2020b, *MNRAS*, 499, 3706 (DOI: 10.1093/mnras/staa3099)
- Michaud G., Alecian G., Richer J., 2015, *Atomic Diffusion in Stars* (Switzerland: Springer International Publishing) (DOI: 10.1007/978-3-319-19854-5)
- Napiwotzki R., Schönberner D., Wenske, V., 1993, *A&A*, 268, 653
- Niemczura E., Murphy S. J., Smalley B., Uytterhoeven K., Pigulski A., Lehmann H., Bowman D. M., Catanzaro G., van Aarle E., et al., 2015, *MNRAS*, 450, 2764 (DOI: 10.1093/mnras/stv528)
- Preston G. W., 1974, *ARA&A*, 12, 257 (DOI: 10.1146/annurev.aa.12.090174.001353)
- Richer J., Michaud G., Turcotte S., 2000, *ApJ*, 529, 338 (DOI: 10.1086/308274)
- Saffe C., Miquelarena P., Alacoria J., Flores M., Jaque Arancibia M., Calvo D., Martín Girardi G., Grosso M., Collado A., 2021, *A&A*, 647, A49 (DOI: 10.1051/0004-6361/202040132)
- Takeda Y., 1991, *A&A*, 242, 455
- Takeda Y., 1995, *PASJ*, 47, 287
- Takeda Y., Han I., Kang D.-I., Lee B.-C., Kim K.-M., 2008, *JKAS*, 41, 83 (DOI: 10.5303/JKAS.2008.41.4.083)

- Takeda Y., Kambe E., Sadakane K., Masuda S., 2010, PASJ, 62, 1239 (DOI: 10.1093/pasj/62.5.1239)
- Takeda Y., Kang D.-I., Han I., Lee B.-C., Kim K.-M., 2009, PASJ, 61, 1165 (DOI: 10.1093/pasj/61.5.1165)
- Takeda Y., Kang D.-I., Han I., Lee B.-C., Kim K.-M., Kawanomoto S., Ohishi N., 2012, PASJ, 64, 38 (DOI: 10.1093/pasj/64.2.38)
- Takeda Y., Kawanomoto S., Ohishi N., 2007, PASJ, 59, 245 (DOI: 10.1093/pasj/59.1.245)
- Takeda Y., Kawanomoto S., Ohishi N., 2014, PASJ, 66, 23 (DOI: 10.1093/pasj/pst024)
- Takeda Y., Kawanomoto S., Ohishi N., Kang D.-I., Lee B.-C., Kim K.-M., Han I., 2018, PASJ, 70, 91 (T18) (DOI: 10.1093/pasj/psy091)
- Takeda Y., Ohkubo M., Sato B., Kambe E., Sadakane K., 2005b, PASJ, 57, 27 (DOI: 10.1093/pasj/57.1.27)
- Takeda Y., Sadakane K., 1997, PASJ, 49, 367 (DOI: 10.1093/pasj/49.3.367)
- Takeda Y., Sato B., Kambe E., Masuda S., Izumiura H., Watanabe E., Ohkubo M., et al., 2005a, PASJ, 57, 13 (DOI: 10.1093/pasj/57.1.13)
- Talon S., Richard O., Michaud G., 2006, ApJ, 645, 634 (DOI: 10.1086/504066)
- van Leeuwen F., 2007, Hipparcos, the New Reduction of the Raw Data, Astrophysics and Space Science Library, Vol. 350 (Berlin: Springer) (DOI: 10.1007/978-1-4020-6342-8)

A. Non-LTE effects on Si II 6347/6371 lines in B-type stars

Recently, Mashonkina (2020a) carried out an extensive study on the non-LTE line formation for silicon (Si I, Si II, and Si III) in main-sequence stars of A- and B-type covering the T_{eff} range between 7000 and 20000 K. Mashonkina’s calculation includes the Si II 6347/6371 lines and the non-LTE corrections for these lines derived by her for late A through late B stars ($T_{\text{eff}} \sim 7000\text{--}13000$ K; negative Δ with extents of several tenths dex) are more or less consistent with the results of this investigation.

However, her calculation failed to explain the formation of these Si II doublet lines in the early B-type star ι Her ($T_{\text{eff}} = 17500$ K), because of the *positive* non-LTE corrections resulting in unacceptably large non-LTE Si abundances ($\Delta_{6347} = +0.60$, $\Delta_{6371} = +0.67$, $A_{6347}^{\text{N}} = 8.38$, $A_{6371}^{\text{N}} = 8.27$; cf. Table 4 in her paper).

Although such an early B-type star is outside of the scope of this study, it is interesting to examine whether similar inconsistency emerges in our calculations at the higher T_{eff} regime (> 15000 K). For this purpose, additional non-LTE calculations were performed for the $\log g = 4$ models with extended T_{eff} up to 20000 K. The resulting runs of $l_0^{\text{NLTE}}/l_0^{\text{LTE}}$ and S_{L}/B with depth for the Si I 6347/6371 lines (from $T_{\text{eff}} = 8000$ K through 20000 K) are depicted in Figs. 10a and 10b; and Figs. 10c and 10d display how W_{6371} and Δ_{6371} (for the weaker line of the doublet) vary with T_{eff} .

Our calculations suggest that the extent of the (negative) non-LTE abundance correction ($|\Delta|$) progressively decreases with an increase of T_{eff} in the regime of B-type stars ($T_{\text{eff}} \gtrsim 10000$ K), until it eventually reaches $\Delta \sim 0$ at the critical T_{eff} of ~ 19000 K; thereafter Δ turns into positive (cf. Fig. 10d). In other words, the line is strengthened by the non-LTE effect ($W^{\text{N}} > W^{\text{L}}$) at $T_{\text{eff}} \lesssim 19000$ K while weakened ($W^{\text{N}} < W^{\text{L}}$) at $T_{\text{eff}} \gtrsim 19000$ K, as can be confirmed in Fig. 10c.

As mentioned in Section 6.1, the behavior of Δ is mainly controlled by the line source function; that is, as long as the inequality $\langle S_{\text{L}} \rangle < \langle B \rangle$ (S_{L} dilution) holds in the line-forming region, Δ remains negative. However, according to Fig. 10b, as T_{eff} is ever increased, $\langle S_{\text{L}} \rangle$ becomes comparable with or even outweighs $\langle B \rangle$, which explains why Δ approaches zero or even turns into positive at higher T_{eff} (~ 20000 K).

Fig. 10d suggests that the non-LTE correction for ι Her ($T_{\text{eff}} = 17500$ K) expected from our calculation is $\Delta_{6371} \sim -0.1$ dex. Then, since the LTE abundance is $A_{6371}^{\text{L}} = 7.60$ (cf. Table 4 in Mashonkina 2020a), the non-LTE Si abundance for ι Her would make $A_{6371}^{\text{N}} \sim 7.5$, which is almost consistent with the solar abundance.

Mashonkina’s (2020a) Δ_{6371} vs. T_{eff} relation (taken from Table 9 of her paper) is also overplotted for comparison in Fig. 10d. We can see from this figure that the upturn of Mashonkina’s Δ_{6371} is considerably steeper and $\Delta_{6371} \sim 0$ is attained already at $T_{\text{eff}} \sim 13000\text{--}14000$ K, which is in marked contrast to our calculation (critical T_{eff} for $\Delta_{6371} \sim 0$ is at ~ 19000 K). The reason for this discrepancy is not clear. An inspection of the bottom panel of Mashonkina’s (2020a) Fig. 1 (in comparison with our Fig. 10a) suggests that Si II levels are largely underpopulated (presumably due to more enhanced Si II overionization) in her calculation. We suspect that her procedure of evaluating UV photoionizing radiation field may have been rather different, for which we used the opacities included in Kurucz’s (1993a) ATLAS9 program along with Kurucz’s (1993b) line opacity distribution function as described in Section 3.1.2 of Takeda (1991).

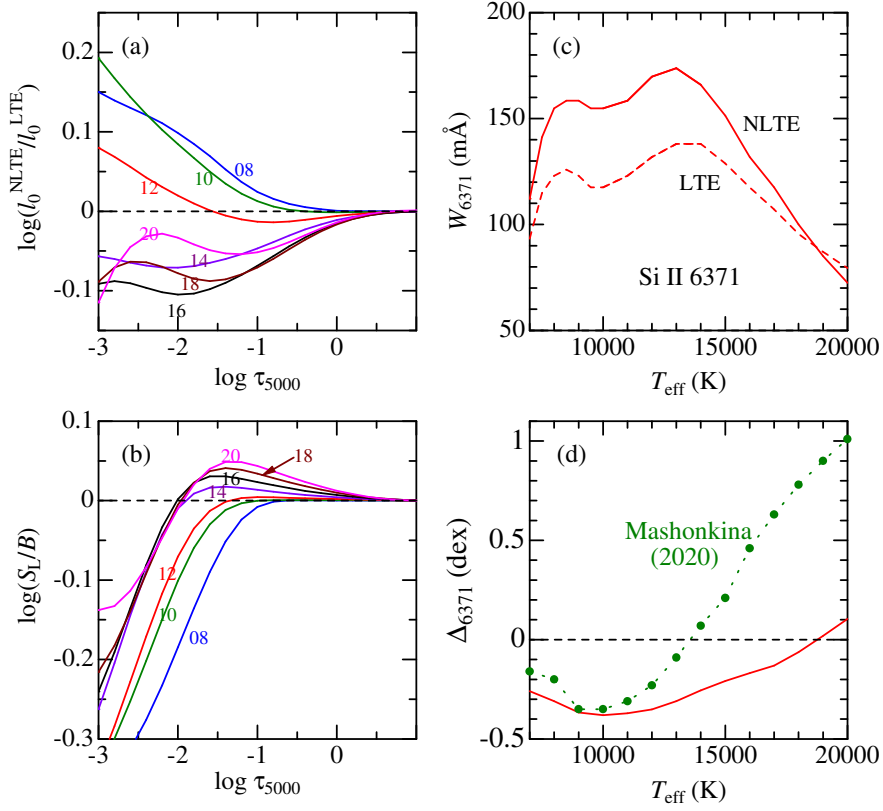






Figure 10. Non-LTE calculation results for the Si II $4s$ ^2S-4p $^2P^\circ$ transition of multiplet 2 (like the case of Figs. 5 and 6), which were derived for $\log g = 4$ models (with $\xi = 2 \text{ km s}^{-1}$ and $[\text{Si}/\text{Fe}] = [\text{Fe}/\text{H}] = 0$) but T_{eff} extended up to 20000 K (in order to cover early B stars). (a) The non-LTE-to-LTE line-center opacity ratio (vs. τ_{5000}), (b) S_L/B ratio (vs. τ_{5000}), (c) non-LTE and LTE equivalent widths for Si II 6371 (vs. T_{eff}), and (d) non-LTE correction for Si II 6371 (vs. T_{eff}). In panels (a) and (b), $T_{\text{eff}}/1000$ is marked in each curve. In panel (d), the T_{eff} -dependence of Δ_{6371} calculated by Mashonkina (2020a) is also shown for comparison.

Distance determination by magnitude analysis of some open clusters with GAIA *era* and stellar luminosity function

W.H. Elsanhoury^{1,2}, Amnah S. Al-Johani³, Noha H. El Fewaty^{2,4} and A.A. Haroon⁵

¹ *Astronomy Department, National Research Institute of Astronomy and Geophysics (NRIAG) 11421, Helwan, Cairo, Egypt*

² *Physics Department, Faculty of Science and Arts, Northern Border University, Turaiif Branch, Saudi Arabia (E-mail: elsanhoury@nbu.edu.sa, welsanhoury@gmail.com)*

³ *Mathematics Department, Faculty of Science, Tabuk University, Saudi Arabia (E-mail: aalgohani@ut.edu.sa, xxwhitelinnnetxx@hotmail.com)*

⁴ *Physics Department, Faculty of Science, Cairo University, Cairo, 12613, Egypt (E-mail: nohah.ahmad@nbu.edu.sa, physicsnbu@gmail.com)*

⁵ *Astronomy and Space Science Department, Faculty of Science, King Abdul Aziz University, Jeddah, Saudi Arabia (E-mail: aaharoon@kau.edu.sa)*

Received: August 17, 2021; Accepted: October 30, 2021

Abstract. In this work, we carry out by utilizing the distance equation with providing some basic descriptive statistics for both apparent and absolute magnitudes, the distances of some open clusters (i.e., Hyades, Pleiades, IC 2391, Kaposov 12, Kaposov 43, NGC 1348, NGC 2112, NGC 4337, SAI 24, and SAI 94) with the assumption that all members N are scattering around a mean absolute magnitude in a Gaussian distribution. Our numerical obtained results are in good agreement with previously calculated values. In the second part of the paper, we have calculated the luminosity function of Hyades open cluster by Salpeter's normalized function $\Psi(M_V)$ due to frequency distribution function $\Phi(M_V)$, on this way, we have got a very significant relationship between them with absolute magnitudes M_V (i.e., the linear correlation coefficient ~ 0.995), and the error analysis are also given.

Key words: Open clusters; Distance equation (Malmquist bias); Density distribution function.

1. Introduction

Open clusters are mostly found in the spiral arms of the Milky Way Galaxy; therefore, they are suitable traces in the studies of Galactic disk and structure (Carraro et al. 1998; Chen et al. 2003; Joshi et al. 2016). Open clusters and/or

stellar associations have been used to determine spiral arm structure, to map the rotation curve of the Galaxy, to investigate the mechanisms of star formation and its recent history, and to constrain the initial luminosity and mass function (LF and MF) in aggregates of stars. Old clusters, and in large distances, are used to define disk abundance gradients, the cluster age-metallicity relationship, point to a complex history of chemical enrichment, and mixing in the disc (Friel 1995).

Particularly, the oldest members with Galactic open clusters, serve as excellent probes of the structure and evolution of the Galactic disk. Individual clusters provide excellent tests of stellar and dynamical evolution.

One of the most important pieces of information needed in astronomy is the distances to the stars or celestial objects. If the distance (r ; pc) of a star is known as well as its proper motion (μ ; mas/yr) then one can calculate its tangential velocity (V_t ; km/s) to the line of sight (Robinson 1985). Also, having measured the distances to the globular clusters, we can study the distribution in the Galaxy (Cassisi et al. 2001; Duncan et al. 2001). In moving clusters if the equatorial coordinates of the vertex and the distance of each member are known, then one can easily determine the velocity of the cluster and the position of its center (Elsanhoury et al. 2013). On the other hand, the determination of distances within our Galaxy allows us to calibrate the distance indicators (Shanks 1997; Borchkhadze and Kogoshvili 1999). Moreover, determining distances would also help astronomers in their quest to understand the size and age of the universe (Willick and Batra 2001; Mazumdar and Narasimha 1990), since it would provide an independent estimation of the size of the first steps on the cosmic distance ladder. Consequently, it contributes to the theories about the origin of the universe.

The purpose of our research work is to compute the distances of some open clusters based on the so-called Malmquist bias with aid of the second Gaia data release Gaia DR2¹ (Cantat-Gaudin and Anders 2020).

The catalog of the second Gaia database release comes to a G-band magnitude for sources brighter than 21 mag (Weiler 2018); i.e., with 9 order of magnitude fainter than Tycho-Gaia Astrometric Solution TGAS (Michalik et al. 2015). At its faint end, the Gaia DR2 astrometric precision is accurate with that of Tycho-Gaia Astrometric Solution TGAS, whereas for stars brighter than $G \lesssim 15$ the precision is about ten times way better than in TGAS, thus allowed to extend membership determination to fainter and more distant objects. For about 1.3 billion sources, the Gaia DR2 catalog devoted to five astrometric parameters solutions; i.e., the central coordinates (α, δ), proper motion in both sides ($\mu_{\alpha*}, \mu_{\delta}$), and the parallaxes (π ; mas). Moreover, Gaia DR2 having three broad bands; G, G_{BP} (Blue Prism), and G_{RP} (Red Prism) photometric magnitudes; i.e., G (330-1050 nm), G_{BP} (330-680 nm), and G_{RP} (630-1050 nm) with precisions at the mmag level.

¹<https://vizier.u-strasbg.fr/viz-bin/VizieR?-source=J/A+A/633/A99>

In the present paper, the data analysis for our program open clusters; i.e., Hyades, Pleiades, IC 2391, Kaposov 12, Kaposov 43, NGC 1348, NGC 2112, NGC 4337, SAI 24, and SAI 94 were achieved with Section 2 and performing computation of the distances with a statistical magnitude analysis. Section 3 deals with the distribution function of the Hyades cluster. Section 3 is dedicated to the conclusion of the study.

2. The distance equation

For our program, open clusters, who's drawn in Table 1; into which the first column presents the cluster names, second column deals with members N (candidates), the Galactic positions (l, b) of these targets devoted here with columns 3 and 4, mean right ascension of members (ICRS) at epoch = 2015.5 and mean declination of members (ICRS) at epoch = 2015.5 are given here with columns 5 and 6, columns 7 and 8 gives the proper motions in both sides ($\mu_{\alpha^*}, \mu_{\delta}$) with errors in units of (mas/yr), and the last column presents the parallaxes (π) with its errors in units of (mas).

let us consider that; all members are on the same distance $r(\text{pc})$ and spread out (scatter) around a mean absolute magnitude (M_o) in a Gaussian distribution with dispersion (σ). Then the probability $p(M)dM$ of a member of the celestial set that has an absolute magnitude in the range ($M \& M+dM$); i.e., frequency distribution function of the absolute magnitudes of the cluster members takes the form (Mihalas and Binney 1981; Scheffler and Elsasser 1988).

$$p(M)dM = \Phi(M) = \frac{1}{\sigma\sqrt{2\pi}} e^{-\frac{(M-M_o)^2}{2\sigma^2}}, -\infty \leq M \leq \infty \quad (1)$$

The distance equation can be written as (Abdel-Rahman et al. 2009)

$$r(\text{pc}) = 10^{\frac{1+(m_1-M_o-y\sigma-A-[Fe/H])}{5}}. \quad (2)$$

where (m_1 ; mag) is the faintest apparent magnitude of the cluster stars, (A) is the magnitude of the interstellar absorption, $[Fe/H]$ is the metallicity, and (y) is the solution of the transcendental equation.

$$\Lambda(y) = y + e^{-\frac{y^2}{2}} \left\{ \sqrt{\frac{\pi}{2}} \left[1 + \text{erf} \left(\frac{y}{\sqrt{2}} \right) \right] \right\}^{-1} - \alpha = 0,$$

and

$$\alpha = \frac{m_1 - \bar{m}}{\sigma}$$

where (\bar{m} ; mag) is the average value of the apparent magnitude.

The distance $r(\text{pc})$ of the observed members that complete down to a fixed limiting magnitude \bar{m} in the absolute range $M, M+dM$ is given by

$$r(\text{pc}) = 10^{1+0.2(\bar{m}-M)}$$

The distance modulus is then given by:

$$(m - M) = m_1 - M_o - y\sigma - A - [Fe/H].$$

Increasing $[Fe/H]$ values affect the luminosity negatively and hence the magnitudes and the distances will increase. The metallicity must be subtracted if positive and neglected when negative.

Table 1. The fundamental parameters of our program open clusters devoted to Gaia DR2 (Cantat-Gaudin and Anders 2020).

Clusters	N	l deg.	b deg.	Ra. deg.	Dec. ^o deg.	$\mu_{\alpha*} \pm \sigma_{\mu_{\alpha*}}$ mas/yr	$\mu_{\delta} \pm \sigma_{\mu_{\delta}}$ mas/yr	$\pi \pm \sigma_{\pi}$ mas
Hyades	197	180.058	-22.349	66.717 ^(b)	15.867 ^(b)	113.630 ^(a)	-26.350 ^(a)	20.00 ^(b)
Pleades	1008	166.462	-23.614	56.601	24.114	20.077±0.035	-45.503±0.038	7.346±0.006
IC 2391	224	270.386	-6.737	130.292	-52.991	-24.644±0.056	23.316±0.049	6.582±0.010
Koposov 12	171	176.155	6.013	90.245	35.287	0.699±0.009	-1.732±0.011	0.396±0.005
Koposov 43	31	179.923	1.747	88.079	29.901	-0.037±0.021	-1.664±0.014	0.18±0.011
NGC 1348	105	146.968	-3.709	53.524	51.409	1.288±0.025	-0.726±0.025	0.404±0.006
NGC 2112	719	205.886	-12.605	88.452	0.403	-2.713±0.009	4.27±0.009	0.877±0.003
NGC 4337	247	299.316	4.555	186.022	-58.125	-8.841±0.006	1.468±0.006	0.357±0.003
SAI 24	130	138.013	1.493	44.816	60.566	-0.201±0.017	0.114±0.017	0.446±0.005
SAI 94	85	265.432	-2.176	131.171	-46.292	-4.254±0.17	4.479±0.017	0.204±0.008

(a) Perryman et al. (1998) (b) Kharchenko et al. (2016)

If we now measure the average absolute magnitude for these members, we will obtain.

$$\overline{M} = \frac{\int p(M)Mr^3 dM}{\int p(M)r^3 dM} = \frac{\int \exp\left\{-\frac{(M-M_o)^2}{2\sigma^2} - 0.6M \ln 10\right\} M dM}{\int \exp\left\{-\frac{(M-M_o)^2}{2\sigma^2} - 0.6M \ln 10\right\} dM} = M_o - 0.6\sigma^2 \ln 10 = M_o - 1.382\sigma^2$$

that is

$$M_o = \overline{M} + 1.382\sigma^2 \quad (3)$$

Therefore the last relation between M_o and σ (Bok 1937) predicts $M_o > \overline{M}$; i.e., the stars one sees at a given absolute magnitude are, on average, more luminous than the average for all the stars in each volume. This effect (i.e., $1.382 \sigma^2$) is called the Malmquist bias, arises because, when one selects stars of fixed absolute magnitude, the volume element containing the more distant, intrinsically luminous stars is larger than that occupied by the nearer, fainter objects. The Malmquist bias too acting an important role in connection with counts of radio Galaxies, quasars, and other objects, that have been used as cosmological probes.

Our computed distances r_c (pc) for our program and those estimated r_e (pc) with different authors are drawn like in Table 2, with formats, column 1 gives the name of the cluster, columns 2 and 3 devoted to faintest and average values of the apparent magnitudes, respectively, column 4 deals with values of the

absolute magnitudes, columns 5 and 6 devoted with dispersion σ and the α , respectively, column 7 gives our computed distances r_c (pc) with its errors (i.e., $\sqrt{\sum (\text{actual value} - \text{predicted value})^2 / N}$), where N is the total number of stars in each cluster, and column 8 represents estimated ones r_e (pc) with different authors as listed in column 9.

Fig. 1 presents a comparison between distances that were computed in our work with our program abscissa (r_c ; kpc) and others as ordinate (r_e ; kpc) with a correlation coefficient $\sim 92\%$. Here its mentioned slightly that no systematic difference is shown among our statistical manipulation method and others.

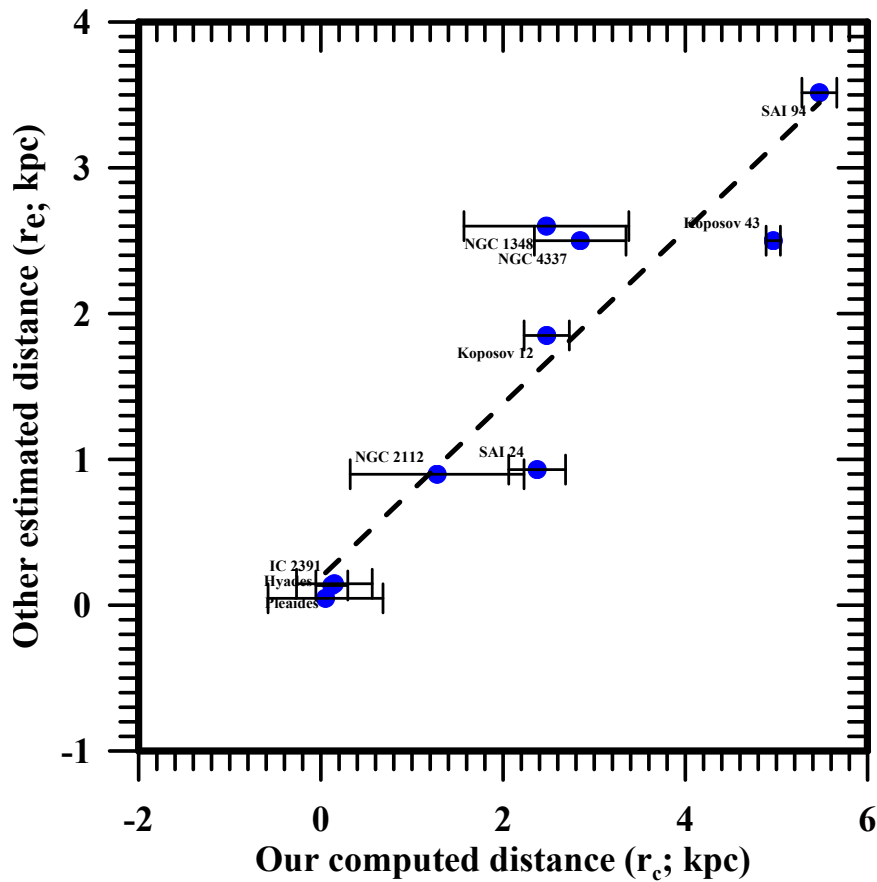


Figure 1. Plot with error bars, showing consistent between our computed distances (abscissa; r_c) as listed in the seventh column of Table 2 with those (ordinate; r_e) obtained by different authors (eighth column). The plot highly showing the correlation coefficient ($\sim 92\%$).

Table 2. Our computed distances r_c (pc) with its uncertainties and other estimated ones r_c (pc) devoted to different authors.

Clusters	m_1 mag	\bar{m} mag	\bar{M} mag	σ mag	α	$r_c \pm \sigma_{r_c}$ pc	r_e pc	Authors
Hyades	11.880	7.851	4.464	2.081	1.936	51.00±0.16	47.00±0.20 47.03±0.20	Elsanhoury and Nouh (2019) Lodieu et al. (2019)
Pleades	17.957	14.756	9.087	2.801	1.144	120.30±1.00	135.00±1.60 134.00	Elsanhoury and Nouh (2019) Galli et al. (2017)
IC 2391	17.980	14.715	8.802	2.838	1.151	148.00±0.27	145±2.50 147±5.50	van Leeuwen (2007) Dodd (2004)
Koposov 12	17.993	15.538	3.512	1.402	1.752	2479.00±8.00	1850±43 2351.20 2525.25 2000 1900 2000±200 2050	Elsanhoury (2021) Soubiran et al. (2018) Cantat-Gaudin et al. (2018) Sampedro et al. (2017) Kharchenko et al. (2013) Yadav et al. (2011) Froebrich et al. (2008)
Koposov 43	17.725	15.896	2.279	1.236	1.481	4965.00±93.00	2500±50 4787.50 5555.56 2800 3000 2800	Elsanhoury (2021) Soubiran et al. (2018) Cantat-Gaudin et al. (2018) Sampedro et al. (2017) Kharchenko et al. (2013) Froebrich et al. (2008)
NGC 1348	17.949	16.072	4.042	1.542	1.218	2475.00±11.00	2600±50 2475.25	Bisht et al. (2021) Cantat-Gaudin et al. (2018)
NGC 2112	17.994	15.896	5.600	1.336	1.572	1276.00±5.00	898±41 940±70	Haroon et al. (2017) Carraro et al. (2008)
NGC 4337	17.940	15.518	3.263	1.241	1.952	2846.00±0.30	2500±70 2801.12	Bisht et al. (2020) Cantat-Gaudin et al. (2018)
SAI 24	17.984	15.211	3.428	1.984	1.398	2374.00±8.00	930±30 1000	Elsanhoury and Amin (2019) Kharchenko et al. (2016)
SAI 94	17.934	16.569	3.025	1.244	1.099	5471.00±4.00	3515±60 3886	Elsanhoury and Amin (2019) Kharchenko et al. (2016)

3. Distribution function

The stellar luminosity function is a description of the relative number of stars of different absolute luminosities. It is often used to describe the stellar content of various parts of the Galaxy or other groups of stars, but it most commonly refers to the absolute number of stars of different absolute magnitudes in the Solar neighborhood. In this form, it is usually called van Rhijn function (van Rhijn 1936).

The detailed determination of the luminosity function of the Solar neighborhood is an extremely complicated process. Difficulties arise because of the incompleteness of existing surveys of stars of all luminosities in any sample of space, and the uncertainties in the basic data (distances and magnitudes).

The effect of stellar evolution on the observed luminosity functions for main-sequence stars, $\Phi(M_V)$ in the Solar neighborhood, were first investigated by (Salpeter 1955). He reasoned that we observe at the present only those stars which were formed less than $T(M_V)$ years ago, where $T(M_V)$ is the lifetime of a star with an absolute magnitude M_V on the main sequence. For stars with $M_V > 3.5$ the lifetime $T(M_V)$ is larger than the age of the Galaxy, so that we observe all the stars ever formed. For stars brighter than $M_V = 3.5$ however, the ratio of the number we see to the number ever formed will be $T(M_V)/T(\text{Galaxy})$ on the assumption of the uniform rate of star formation. Thus if $\Psi(M_V)$ is the luminosity function of all-stars ever formed in the Solar neighborhood; i.e., initial luminosity function and time-dependent (Miller and Scalo 1979), then the observed luminosity function is given by,

$$\Phi(M_V) = \frac{\Psi(M_V)T(M_V)}{T(\text{Galaxy})}. \quad (4)$$

Where $T(\text{Galaxy})$ is a mean lifetime of the Galaxy.

Salpeter's work is of great importance since it gives a means of predicting the numbers of stars at any given luminosity which have been formed in the lifetime of the Galaxy. The present-day luminosity function of the open clusters within the Solar neighborhood (e.g. Hyades) predicts contains ≈ 25 -30 white dwarfs (Chin and Stothers 1971). The discrepancy between the observed and a predicted number of these objects is possibly explained by evaporation from the cluster (Weidemann et al. 1992; Eggen 1993). One possible example of an escaped white dwarf is the P98 candidate HIP 12031 (DAwe...). It is located beyond 40 pc from the cluster center and is possibly a kinematic member.

In what follows, we focused on the Hyades open cluster (600 Myr), the data were excluded (i.e., 197 stars as members) with Hipparcos data by (Perryman et al. 1998)², which based on observations made with the ESA Hipparcos astrometry satellite. According to (Salpeter 1955) and to obtain $\Psi(M_V)$ from $\Phi(M_V)$, we need only the bolometric magnitude ($M_{bol.}$) and the mass (M/M_\odot) of the

²<https://vizier.u-strasbg.fr/viz-bin/VizieR?-source=J/A+A/331/81>

Table 3. Luminosity function for the Hyades ($\sum N = 197$).

M_V	Observed	$\Phi(M_V)$	$\Psi(M_V)$
3.0 3.5	1	0.165	2.575
3.5 4.0	4	0.301	2.916
4.0 4.5	6	0.529	3.256
4.5 5.0	5	0.893	3.608
5.0 5.5	10	1.44	3.992
5.5 6.0	15	2.213	4.432
6.0 6.5	11	3.23	4.95
6.5 7.0	14	4.474	5.564
7.0 7.5	15	5.875	6.276
7.5 8.0	21	7.324	7.072
8.0 8.5	16	8.691	7.914
8.5 9.0	19	9.862	8.746
9.0 9.5	18	10.777	9.504
9.5 10.0	12	11.442	10.144
10.0 10.5	10	11.937	10.665
10.5 11.0	10	12.395	11.128
11.0 11.5	6	12.989	11.662
11.5 12.0	4	13.914	12.456

stars at a given M_V .

$$\log \Psi(M_V) = \log \Phi(M_V) + 0.4(3.50 - M_{bol.}) - \log \frac{M}{M_\odot} + 0.12 \quad (5)$$

The distribution of luminosities for Hyades open cluster is shown in Table 3, together with the normalized $\Psi(M_V)$ and $\Phi(M_V)$ functions. The luminosity function for Hyades open cluster is shown in Fig. 2, the normalized Salpeter's function is $\Psi(M_V)$ shown as a solid line, while $\Phi(M_V)$ is represented by the dashed line. The fit of $\Psi(M_V)$ to the Hyades cluster is better than $\Phi(M_V)$. This finding supports that the stars in clusters, as well as single stars, obey nearly the same distribution law.

From the formulations of the above section, data of Salpeter's luminosity function $\Psi(M_V)$, and frequency distribution function $\Phi(M_V)$, we get a very significant relationship between them with an absolute magnitude M_V , this relation is given as

$$\Delta_{\text{obs.}} = C_1 + C_2 M_V, \quad (6)$$

where

$$\Delta_{\text{obs.}} = \Phi(M_V) - \Psi(M_V). \quad (7)$$

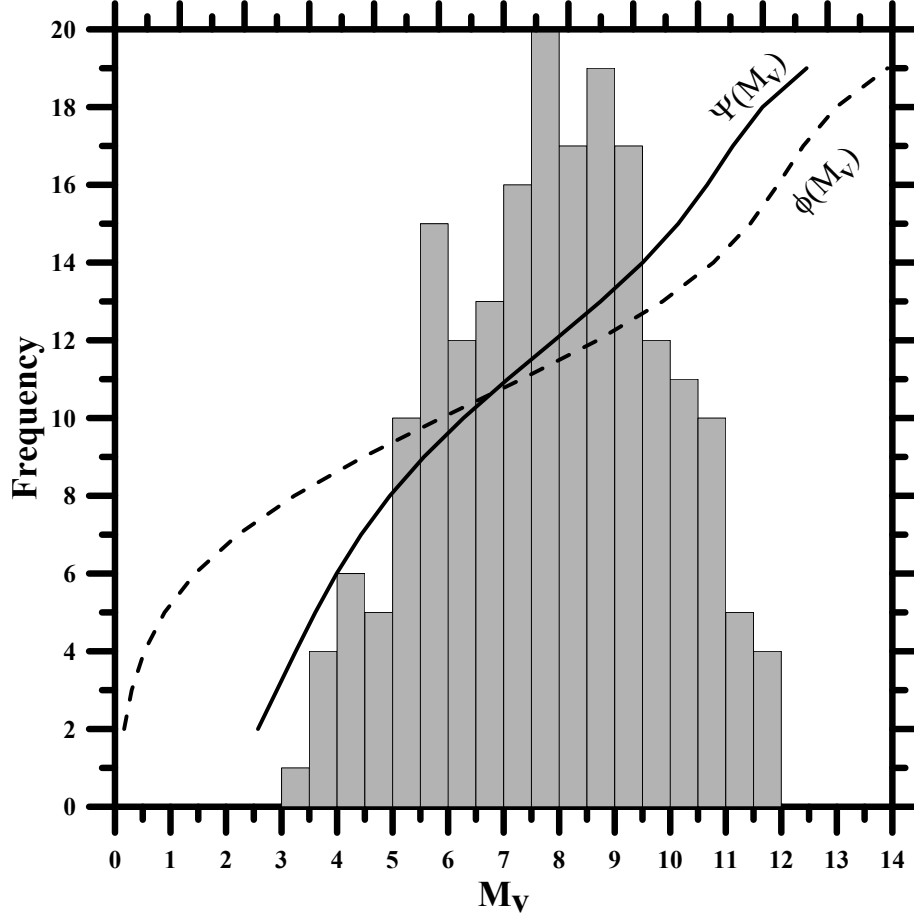


Figure 2. Histograms of the luminosity functions of the Hyades open cluster. The solid line is Salpeter's normalized $\Psi(M_V)$. The dashed line is the normalized general luminosity function $\Phi(M_V)$.

where the coefficients and their probable errors are

- $C_1 = 3.034 \pm 0.163$
- $C_2 = -0.552 \pm 0.026$
- The probable error of the fit is $e = 0.383$
- The average squared distance between the exact solution and the least-squares solution $Q = 0.053$ (Kopal and Sharaf 1980)
- The linear correlation coefficient between (Δ, M_V) is $r = 0.955$
- The graphical representation of the raw data and the fitted data with its absolute relative errors (i.e., $\Delta = \left| \frac{\Delta_{obs.} - \Delta_{cal.}}{\Delta_{cal.}} \right|$) was given in Fig. 3, where $\Delta_{obs.}$

and $\Delta_{cal.}$ are those obtained from Equations (7) and (8), respectively.

$$\Delta_{cal.} = \Psi(M_V) - \Phi(M_V). \quad (8)$$

Some statistical analyses of these errors are given as follows:

- Mean (average value) = 0.675
- Median (central value) = 0.330
- Median absolute deviation = median of $|\Delta_i - \text{median}| = 0.213$
- Root mean square = $\sqrt{\frac{1}{N} \sum_{n=1}^N (\Delta_i)^2} = 1.147$
- Variance = $\frac{1}{N} \sum_{n=1}^N (\Delta_i - \bar{\Delta})^2 = 0.899$
- Mean absolute deviation = $\frac{1}{N} \sum_{n=1}^N |\Delta_i - \bar{\Delta}| = 0.583$

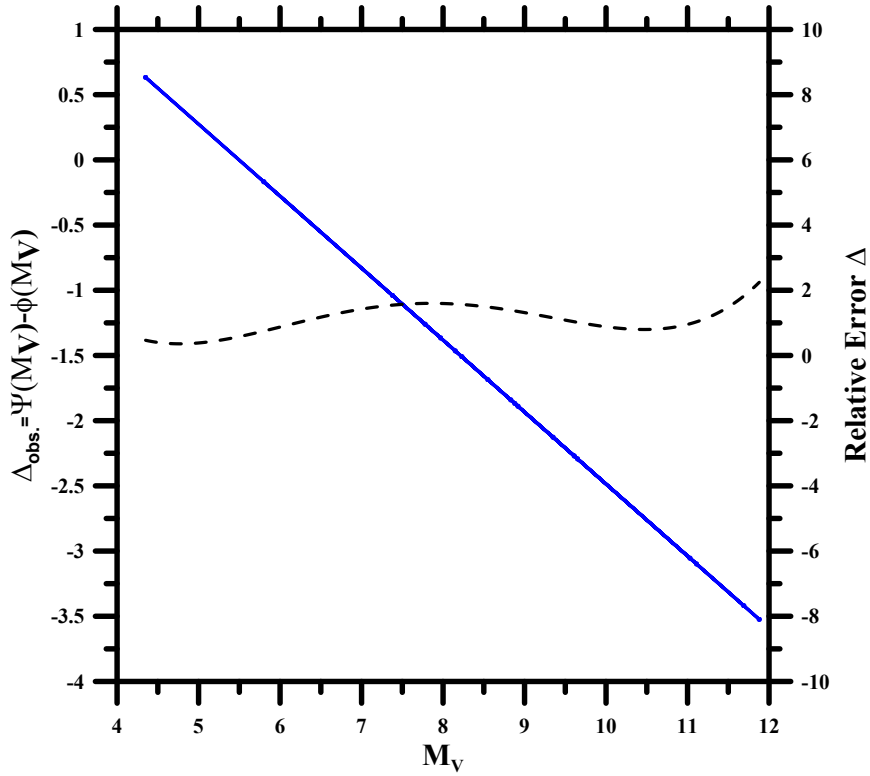


Figure 3. The graphical representation between the $\Delta_{obs.}$ vs. M_V (solid line), with its relative errors (dashed line).

4. Conclusion

Generally, this paper is divided into two folds:

- Utilizing the distance equation, we have computed the distances $r_c(\text{pc})$ for some open clusters. Malmquist started by assuming that the luminosity function is scattered around a mean absolute magnitude M_o in a Gaussian distribution with dispersion σ . Although the distances calculated here are statistically devoted with magnitude analysis, they are in good agreement with other published ones ($\sim 92\%$). We must mention that $r_e(\text{pc})$ obtained mostly photometrically which is affected by so many factors including evolutionary factors. On the other hand, and depending on statistical distribution functions, although based on averages, can give smearing out of some defects that are inherited in other distances.

- We have computed the observed luminosity function $\Phi(M_V)$ and Salpeter's normalized $\Psi(M_V)$ for the Hyades open cluster ($\sum N = 197$) with regarding the bolometric magnitude M_{bol} . It is found that the Salpeter luminosity function is fitted better to the observed frequency distribution of Hyades.

Acknowledgements. The authors deeply thank the anonymous referees for his/her constructive comments that significantly improved the quality of the paper.

This work presents results from the European Space Agency (ESA) space mission Gaia. Gaia data are being processed by the Gaia Data Processing and Analysis Consortium (DPAC). Funding for the DPAC is provided by national institutions, in particular the institutions participating in the Gaia Multi-Lateral Agreement (MLA). The Gaia mission website is <https://www.cosmos.esa.int/gaia>. The Gaia archive website is <https://archives.esac.esa.int/gaia>. This research has made use of the VizieR catalog access tool, CDS, Strasbourg, France (DOI: 10.26093/cds/vizieR).

References

- Abdel-Rahman, H. I., Issa, I. A., Sharaf, M. A., et al., Statistical Gaussian Distribution Function as a Distance Indicator to Stellar Groups. 2009, *Journal of Korean Astronomical Society*, **42**, 71, DOI: 10.5303/JKAS.2009.42.4.071
- Bisht, D., Elsanhoury, W. H., Zhu, Q., et al., An Investigation of Poorly Studied Open Cluster NGC 4337 Using Multicolor Photometric and Gaia DR2 Astrometric Data. 2020, *Astronomical Journal*, **160**, 119, DOI: 10.3847/1538-3881/ab9ffd
- Bisht, D., Zhu, Q., Elsanhoury, W. H., et al., Detailed analysis of the poorly studied northern open cluster NGC 1348 using multi-color photometry and GAIA EDR3 astrometry. 2021, *Publications of the ASJ*, **73**, 677, DOI: 10.1093/pasj/psab029
- Bok, B. J. 1937, *The Distribution of the Stars in Space*

- Borchkhadze, T. M. & Kogoshvili, N. G., Concerning the errors arising through the use of Tully-Fisher relation for estimation of the Virgo cluster distance. 1999, *Astrophysics*, **42**, 25, DOI: 10.1007/BF02700910
- Cantat-Gaudin, T. & Anders, F., Clusters and mirages: cataloguing stellar aggregates in the Milky Way. 2020, *Astronomy and Astrophysics*, **633**, A99, DOI: 10.1051/0004-6361/201936691
- Cantat-Gaudin, T., Jordi, C., Vallenari, A., et al., A Gaia DR2 view of the open cluster population in the Milky Way. 2018, *Astronomy and Astrophysics*, **618**, A93, DOI: 10.1051/0004-6361/201833476
- Carraro, G., Ng, Y. K., & Portinari, L., On the Galactic disc age-metallicity relation. 1998, *Monthly Notices of the RAS*, **296**, 1045, DOI: 10.1046/j.1365-8711.1998.01460.x
- Carraro, G., Villanova, S., Demarque, P., Moni Bidin, C., & McSwain, M. V., The old open cluster NGC 2112: updated estimates of fundamental parameters based on a membership analysis†. 2008, *Monthly Notices of the RAS*, **386**, 1625, DOI: 10.1111/j.1365-2966.2008.13143.x
- Cassisi, S., De Santis, R., & Piersimoni, A. M., The distance to Galactic globular clusters through RR Lyrae pulsational properties. 2001, *Monthly Notices of the RAS*, **326**, 342, DOI: 10.1046/j.1365-8711.2001.04613.x
- Chen, L., Hou, J. L., & Wang, J. J., On the Galactic Disk Metallicity Distribution from Open Clusters. I. New Catalogs and Abundance Gradient. 2003, *Astronomical Journal*, **125**, 1397, DOI: 10.1086/367911
- Chin, C.-W. & Stothers, R., Low-Mass White Dwarfs and the Cooling Sequences in the Hyades Cluster. 1971, *Astrophysical Journal*, **163**, 555, DOI: 10.1086/150800
- Dodd, R. J., Data mining in the young open cluster IC2391. 2004, *Monthly Notices of the RAS*, **355**, 959, DOI: 10.1111/j.1365-2966.2004.08378.x
- Duncan, D., Chaboyer, B., Carney, B., et al., Anchoring the Population II Distance Scale: Accurate Ages for Globular Clusters and Field Halo Stars. 2001, in American Astronomical Society Meeting Abstracts, Vol. **198**, *American Astronomical Society Meeting Abstracts #198*, 63.09
- Eggen, O. J., Degenerate Stars in the Hyades Supercluster. 1993, *Astronomical Journal*, **106**, 642, DOI: 10.1086/116670
- Elsanhoury, W. H., Photometric and kinematical analysis of Kopenov 12 and Kopenov 43 open clusters. 2021, *Journal of Astrophysics and Astronomy*, **42**, 90, DOI: 10.1007/s12036-021-09771-x
- Elsanhoury, W. H. & Amin, M. Y., Photometric Analysis of Newly Discovered Open Clusters SAI 24 and SAI 94 Based on PPMXL Catalogue. 2019, *Serbian Astronomical Journal*, **198**, 45, DOI: 10.2298/SAJ1998045E
- Elsanhoury, W. H. & Nouh, M. I., PPMXL and Gaia morphological analysis of Melotte 22 (Pleiades) and Melotte 25 (Hyades). 2019, *New Astronomy*, **72**, 19, DOI: 10.1016/j.newast.2019.04.006

- Elsanhoury, W. H., Sharaf, M. A., Nouh, M. I., & Saad, A. S., The Kinematics and Velocity Ellipsoid Parameters of Open Star Clusters. 2013, *The Open Astronomy Journal*, **6**, 1
- Friel, E. D., The Old Open Clusters Of The Milky Way. 1995, *Annual Review of Astron and Astrophys*, **33**, 381, DOI: 10.1146/annurev.aa.33.090195.002121
- Froebrich, D., Meusinger, H., & Scholz, A., NTT follow-up observations of star cluster candidates from the FSR catalogue. 2008, *Monthly Notices of the RAS*, **390**, 1598, DOI: 10.1111/j.1365-2966.2008.13849.x
- Galli, P. A. B., Moraux, E., Bouy, H., et al., A revised moving cluster distance to the Pleiades open cluster. 2017, *Astronomy and Astrophysics*, **598**, A48, DOI: 10.1051/0004-6361/201629239
- Haroon, A. A., Ismail, H. A., & Elsanhoury, W. H., Photometric and Kinematic Properties of the Nearby Open Star Cluster NGC 2112. 2017, *Astrophysics*, **60**, 173, DOI: 10.1007/s10511-017-9473-x
- Joshi, Y. C., Dambis, A. K., Pandey, A. K., & Joshi, S., Study of open clusters within 1.8 kpc and understanding the Galactic structure. 2016, *Astronomy and Astrophysics*, **593**, A116, DOI: 10.1051/0004-6361/201628944
- Kharchenko, N. V., Piskunov, A. E., Schilbach, E., Röser, S., & Scholz, R. D., Global survey of star clusters in the Milky Way. II. The catalogue of basic parameters. 2013, *Astronomy and Astrophysics*, **558**, A53, DOI: 10.1051/0004-6361/201322302
- Kharchenko, N. V., Piskunov, A. E., Schilbach, E., Röser, S., & Scholz, R. D., Global survey of star clusters in the Milky Way. V. Integrated JHK_S magnitudes and luminosity functions. 2016, *Astronomy and Astrophysics*, **585**, A101, DOI: 10.1051/0004-6361/201527292
- Kopal, Z. & Sharaf, M. A., Linear Analysis of the Lightcurves of Eclipsing Variables - Part One - Analysis of the Fractional Loss of Light. 1980, *Astrophysics and Space Science*, **70**, 77, DOI: 10.1007/BF00641665
- Lodieu, N., Pérez-Garrido, A., Smart, R. L., & Silvotti, R., A 5D view of the α Per, Pleiades, and Praesepe clusters. 2019, *Astronomy and Astrophysics*, **628**, A66, DOI: 10.1051/0004-6361/201935533
- Mazumdar, A. & Narasimha, D., Distance to the Virgo cluster and estimation of the Hubble Constant. 1999, *Bulletin of the Astronomical Society of India*, **27**, 267
- Michalik, D., Lindegren, L., & Hobbs, D., The Tycho-Gaia astrometric solution . How to get 2.5 million parallaxes with less than one year of Gaia data. 2015, *Astronomy and Astrophysics*, **574**, A115, DOI: 10.1051/0004-6361/201425310
- Mihalas, D. & Binney, J. 1981, *Galactic astronomy. Structure and kinematics*
- Miller, G. E. & Scalo, J. M., The Initial Mass Function and Stellar Birthrate in the Solar Neighborhood. 1979, *Astrophysical Journal, Supplement*, **41**, 513, DOI: 10.1086/190629
- Perryman, M. A. C., Brown, A. G. A., Lebreton, Y., et al., The Hyades: distance, structure, dynamics, and age. 1998, *Astronomy and Astrophysics*, **331**, 81

- Rowan-Robinson, M. 1985, *The cosmological distance ladder : distance and time in the universe*
- Salpeter, E. E., The Luminosity Function and Stellar Evolution. 1955, *Astrophysical Journal*, **121**, 161, DOI: 10.1086/145971
- Sampedro, L., Dias, W. S., Alfaro, E. J., Monteiro, H., & Molino, A., A multimembership catalogue for 1876 open clusters using UCAC4 data. 2017, *Monthly Notices of the RAS*, **470**, 3937, DOI: 10.1093/mnras/stx1485
- Scheffler, H. & Elsasser, H., Book-Review - Physics of the Galaxy and Interstellar Matter. 1988, *Science*, **240**, 1680
- Shanks, T., A test of Tully-Fisher distance estimates using Cepheids and SNIa. 1997, *Monthly Notices of the RAS*, **290**, L77, DOI: 10.1093/mnras/290.4.L77
- Soubiran, C., Cantat-Gaudin, T., Romero-Gómez, M., et al., Open cluster kinematics with Gaia DR2. 2018, *Astronomy and Astrophysics*, **619**, A155, DOI: 10.1051/0004-6361/201834020
- van Leeuwen, F., Validation of the new Hipparcos reduction. 2007, *Astronomy and Astrophysics*, **474**, 653, DOI: 10.1051/0004-6361:20078357
- van Rhijn, P. J., The Absorption of Light in Interstellar Galactic Space and the Galactic Density Distribution. 1936, *Publications of the Kapteyn Astronomical Laboratory Groningen*, **47**, 1
- Weidemann, V., Jordan, S., Iben, J., & Casertano, S., White Dwarfs in the Halo of the Hyades Cluster: The Case of the Missing White Dwarfs. 1992, *Astronomical Journal*, **104**, 1876, DOI: 10.1086/116364
- Weiler, M., Revised Gaia Data Release 2 passbands. 2018, *Astronomy and Astrophysics*, **617**, A138, DOI: 10.1051/0004-6361/201833462
- Willick, J. A. & Batra, P., A Determination of the Hubble Constant from Cepheid Distances and a Model of the Local Peculiar Velocity Field. 2001, *Astrophysical Journal*, **548**, 564, DOI: 10.1086/319005
- Yadav, R. K. S., Glushkhova, E. V., Sariya, D. P., et al., Optical photometric study of the open clusters Kaposov 12, Kaposov 53 and Kaposov 77. 2011, *Monthly Notices of the RAS*, **414**, 652, DOI: 10.1111/j.1365-2966.2011.18430.x

Photometric observations of SN 2017egm and peculiar transient AT 2018cow

D.Yu. Tsvetkov¹, I.M. Volkov^{1,2}, S.Yu. Shugarov^{1,3}, V.G. Metlov¹,
N.N. Pavlyuk¹, O.V. Vozyakova¹ and N.I. Shatsky¹

¹ *Sternberg Astronomical Institute, M.V. Lomonosov Moscow State University, Universitetsky pr. 13, 119234 Moscow, Russia*

² *Institute of Astronomy of the Russian Academy of Sciences, 48 Pyatnitskaya street, 119017 Moscow, Russia*

³ *Astronomical Institute of the Slovak Academy of Sciences 059 60 Tatranská Lomnica, The Slovak Republic*

Received: November 19, 2021; Accepted: December 17, 2021

Abstract. We present 57 photometric epochs of superluminous SN 2017egm in NGC3191, covering the period of 285 days, and 36 epochs of peculiar object AT 2018cow, for which observations lasted 69 days. *UBVRI* photometry was carried out with 7 telescopes at 5 locations, including the 2.5-m telescope at the Caucasus Mountain Observatory of the Sternberg Astronomical Institute. The light and color curves of SN 2017egm were compared to several well-studied objects of similar type. The light curves of SN 2017egm show definite undulations: a shoulder at phase 114 days past maximum and a plateau lasting for a phase interval 155–235 days. We determined the basic parameters of the light curves for SN 2017egm and AT 2018cow: dates and magnitudes of maximum light, rates of decline at different stages of evolution in different bands.

Key words: supernovae: individual (SN 2017egm, AT 2018cow)

1. Introduction

Modern wide-field untargeted surveys resulted in discovery of new and rare types of transients. One of the most important was the discovery of stellar explosions with peak absolute magnitudes $M \leq -21$ mag, which are called superluminous SNe (SLSNe). SLSNe have been found to be divided into two major classes, hydrogen rich and hydrogen poor events: SLSNe-II, SLSNe-I (Quimby et al., 2011). SLSNe-I are among the least understood class of SNe. The explosion mechanism, the sources of energy supply and the nature of the progenitor stars are still debated (Gal-Yam, 2019).

Another interesting new class of objects is the fast blue optical transients (FBOTs) (Margutti et al., 2019). These events are characterized by fast rise (less than 5 days) and decay times, high peak luminosities ($M < -20$ mag), persistent blue colors throughout the decay, featureless spectrum at maximum light and luminous radio counterpart. The nature of these objects is debated, the

proposed models include the failed-supernova scenario, in which the transient is produced by a jet driven by fallback accretion onto a black hole (Soker & Gilkis, 2018), a tidal disruption event (Kuin et al., 2019), a peculiar type Ibn supernova (Perley et al., 2019; Xiang et al., 2021; Pellegrino et al., 2021), but there is a possibility that they represent a new astrophysical phenomenon.

SN 2017egm (Gaia17biu) was discovered by the Photometric Science Alert Team of the Gaia mission on 2017-05-23.9 UT at 16.7 mag ¹. The object was located at $\alpha = 10^{\text{h}}19^{\text{m}}05^{\text{s}}.62$, $\delta = +46^{\circ}27'14''.08$ (J2000), that is $5''.1$ East and $0''.8$ South from the center of the parent galaxy NGC 3191, in the spiral arm. It was classified as a type II SN (Xiang et al., 2017), but later spectroscopic observations revealed the "W-shape" OII broad absorption features, and the SN was reclassified as SLSN-I (Dong et al., 2017). The photometric and spectroscopic monitoring of this object was reported by Bose et al. (2018), Nicholl et al. (2017), Hosseinzadeh et al. (2021). The polarimetry was collected by Maund et al. (2019), Saito et al. (2020). The parent galaxy was studied by Nicholl et al. (2017), Izzo et al. (2018). The circumstellar interaction model for the bolometric light curve was proposed by Wheeler et al. (2017).

Optical transient AT 2018cow was discovered by ATLAS (Smartt et al., 2018) on 2018-06-16.44 UT at 14.76 mag in the ATLAS *o*-band and was located at $\alpha = 16^{\text{h}}16^{\text{m}}00^{\text{s}}.223$ $\delta = +22^{\circ}16'04''.83$ (J2000). The offsets from the center of the parent galaxy CGCG 137-068 were $3''.46$ South and $4''.86$ West.

The object has all observational characteristics of FBOT and several remarkable features: near-relativistic ejecta velocities at early times (Perley et al., 2019); luminous and fast-varying X-ray emission (Rivera Sandoval et al., 2018); high-velocity emission lines of hydrogen and helium emerging at late times (Perley et al., 2019).

AT 2018cow was intensively studied by numerous groups of researchers. Multiwavelength observations were reported by Yamanaka et al. (2018), Benetti et al. (2018), Perley et al. (2019) Prentice et al. (2018), Kuin et al. (2019), Margutti et al. (2019), Nayana & Chandra (2021), Bietenholz et al. (2020), Rivera Sandoval et al. (2018), Xiang et al. (2021).

The host galaxy and environment of AT 2018cow was studied by Lyman et al. (2020), Michałowski et al. (2019), Roychowdhury et al. (2019).

These analyses have proposed different interpretations of the progenitor, including a tidal disruption event in an intermediate mass black hole, a magnetar, and the electron capture of a merged white dwarf. A supernova origin was also considered, and similarities to the type IIn and Ibn SNe were found by Perley et al. (2019), Xiang et al. (2021), Pellegrino et al. (2021). The model of circumstellar interaction of a pulsational pair-instability SN was proposed by Leung et al. (2020).

¹<https://wis-tns.weizmann.ac.il/object/2017egm/>

2. Observations and data reduction

Photometric observations of SN 2017egm and AT 2018cow were carried out with the 2.5-m telescope of Caucasus Mountain observatory of SAI (K250) (Potanin et al., 2017), 1-m and 0.6-m telescopes of Simeiz Observatory of Crimean Astrophysical Observatory (S100, S60) (Nikolenko et al., 2019), 0.6-m telescope of Crimean Observatory of SAI (C60), 0.6-m telescope of the Stará Lesná Observatory of the Astronomical Institute of the Slovak Academy of Sciences (L60), 0.7-m and 0.2-m telescopes of SAI in Moscow (M70, M20).

The review of the photometric program and our preliminary data on SN 2017egm are presented by Tsvetkov et al. (2019).

The standard image reductions and photometry were made using the IRAF². The magnitudes of the SN were derived by a PSF-fitting relatively to a sequence of local standard stars.

The CCD image of SN 2017egm and local standard stars is presented in Fig. 1, and the image of AT 2018cow is shown in Fig. 2.

The magnitudes of the local standards were obtained from the APASS³ and SDSS⁴ databases, the magnitudes in the *ugri* bands were transformed to the Johnson-Cousins *UBVRI* system using relations by Chonis & Gaskell (2008). The magnitudes of the stars around SN 2017egm are presented in Table 1, and those for AT 2018cow are listed in Table 3.

Table 1. *UBVRI* magnitudes of local standard stars for SN 2017egm

Star	<i>U</i>	σ_U	<i>B</i>	σ_B	<i>V</i>	σ_V	<i>R</i>	σ_R	<i>I</i>	σ_I
1	13.08	0.03	12.22	0.02	11.18	0.01	10.65	0.02	10.16	0.02
2	14.37	0.05	14.28	0.04	13.61	0.01	13.26	0.01	12.90	0.02
3	14.99	0.03	14.77	0.02	14.06	0.01	13.69	0.01	13.32	0.02
4	16.82	0.06	16.04	0.06	15.06	0.03	14.46	0.04	13.91	0.03
5	16.18	0.06	16.34	0.05	15.94	0.04	15.71	0.04	15.39	0.03
6	19.11	0.08	17.96	0.09	16.54	0.04	15.65	0.04	14.80	0.05

The surface brightness of the host galaxy at the location of the SN 2017egm is high, and subtraction of the galaxy background was necessary for accurate photometry. For AT 2018cow the influence of the background is smaller, but we also applied image subtraction. We used the SDSS images, which were transformed and subtracted using standard IRAF routines.

²IRAF is distributed by the National Optical Astronomy Observatory, which is operated by AURA under cooperative agreement with the National Science Foundation.

³<https://www.aavso.org/download-apass-data>

⁴<http://skyserver.sdss.org/dr16/en/tools/search/radial.aspx>

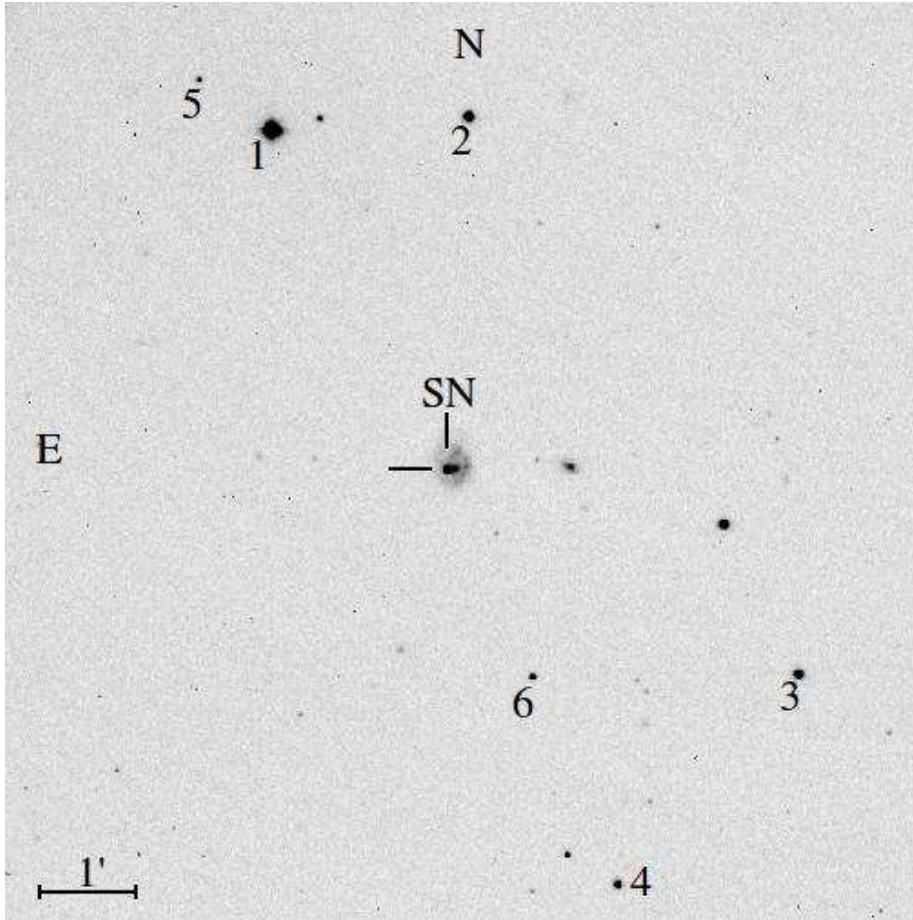


Figure 1. The image of SN 2017egm and local standard stars

The photometry was transformed to the standard Johnson-Cousins system by means of instrumental color-terms, determined from observations of standard star clusters.

Our photometry of SN 2017egm is presented in Table 2, and the results for AT 2018cow are reported in Table 4.

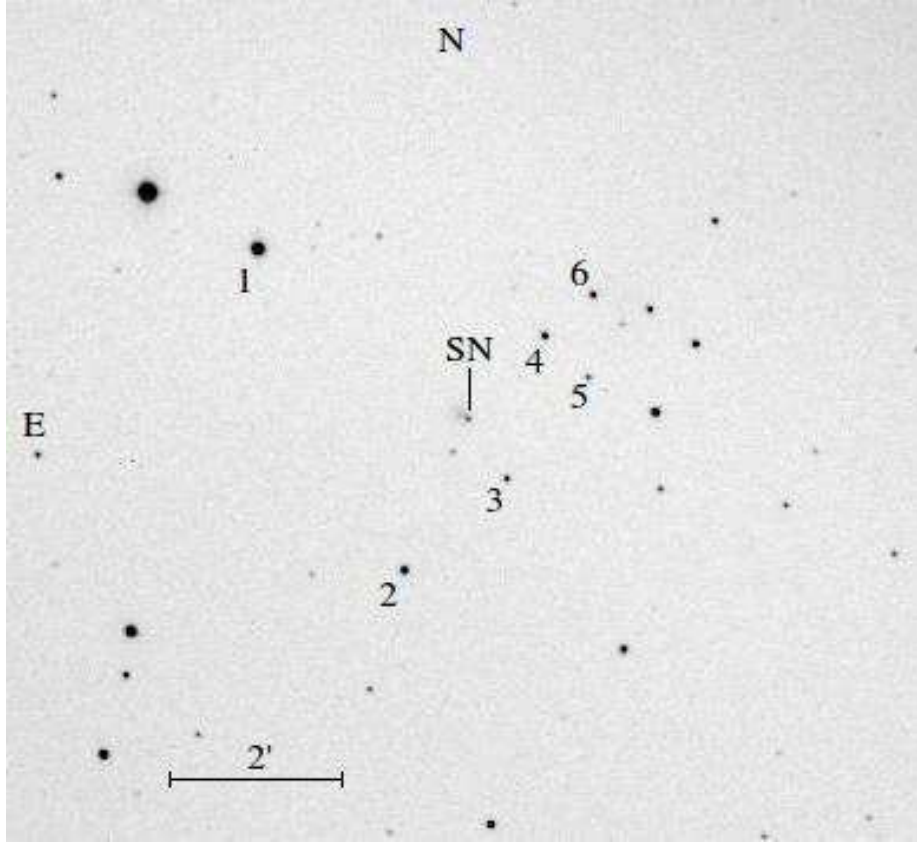


Figure 2. The image of AT 2018cow and local standard stars

Table 2.: *UBVRI* photometry of SN 2017egm

JD– 2450000	<i>U</i>	σ_U	<i>B</i>	σ_B	<i>V</i>	σ_V	<i>R</i>	σ_R	<i>I</i>	σ_I	Tel.
7924.29			14.79	0.03	14.81	0.02	14.88	0.02	14.88	0.03	S100
7925.28			14.80	0.03	14.79	0.02	14.84	0.02	14.84	0.03	S100
7926.29			14.81	0.03	14.78	0.02	14.83	0.02	14.82	0.03	S100
7926.36							14.81	0.03			L60
7927.28			14.79	0.04	14.78	0.02	14.83	0.02	14.77	0.03	S100
7928.28			14.81	0.03	14.78	0.01	14.81	0.01	14.83	0.03	S100
7929.29			14.84	0.03	14.82	0.02	14.83	0.02	14.82	0.05	S100
7929.36	14.09	0.05	14.95	0.04	14.80	0.01	14.83	0.02	14.83	0.02	L60
7930.29			14.86	0.03	14.81	0.01	14.83	0.02	14.81	0.03	S100

Table 2.: Continued.

JD–	U	σ_U	B	σ_B	V	σ_V	R	σ_R	I	σ_I	Tel.
2450000											
7931.28			14.88	0.03	14.88	0.01	14.86	0.02	14.81	0.02	S100
7932.28			14.94	0.03	14.86	0.01	14.89	0.01	14.85	0.03	S100
7933.28			14.94	0.03	14.90	0.02	14.89	0.02	14.84	0.03	S100
7934.28			14.97	0.04	14.90	0.01	14.89	0.02	14.84	0.03	S100
7938.30	14.25	0.03	15.03	0.02	14.94	0.01	14.89	0.01			K250
7940.28			15.11	0.04	15.01	0.02	14.95	0.01	14.81	0.02	S100
7941.27			15.10	0.04	14.99	0.02	14.93	0.02	14.83	0.02	S100
7942.28			15.12	0.04	15.01	0.02	14.96	0.02	14.85	0.02	S100
7943.28			15.08	0.05	15.01	0.01	14.97	0.01	14.85	0.02	S100
7944.28			15.06	0.04	15.00	0.01	15.01	0.02	14.82	0.03	S100
7945.28			15.15	0.04	15.04	0.02	15.00	0.02	14.88	0.03	S100
7946.28			15.14	0.04	15.01	0.02	14.98	0.02	14.83	0.02	S100
7947.26			15.21	0.05							K250
7948.27	14.37	0.11	15.23	0.05	15.11	0.04	15.01	0.05	14.90	0.04	K250
7949.29	14.34	0.12	15.20	0.05	14.99	0.02	14.91	0.04	14.80	0.14	K250
7949.29					15.08	0.02	14.92	0.01			S60
7952.29	14.39	0.14	15.18	0.05	15.01	0.02	14.94	0.04	14.79	0.12	K250
7953.25	14.56	0.08	15.27	0.05	15.08	0.03	15.02	0.04	14.88	0.12	K250
7955.26	14.54	0.09	15.27	0.05	15.08	0.03	15.01	0.04	14.90	0.04	K250
7955.32			15.44	0.05	14.99	0.02	15.00	0.02	14.82	0.02	S60
7956.29			15.47	0.07	15.11	0.03	15.06	0.02			S60
7966.30							15.09	0.06			M20
7969.29					15.35	0.05	15.01	0.04			M20
7981.25					15.57	0.04	15.38	0.03			S100
7981.30			15.80	0.14	15.59	0.11	15.38	0.04			M20
7985.23							15.58	0.05	15.13	0.07	S100
7986.24			15.99	0.09	15.63	0.03	15.52	0.03	15.23	0.03	S100
7991.24							15.66	0.04			S60
7991.58					15.84	0.05	15.55	0.03	15.29	0.03	C60
7992.57			16.31	0.07	15.81	0.03	15.67	0.03	15.35	0.05	C60
7993.58			16.36	0.07	15.80	0.02	15.58	0.03	15.36	0.07	C60
7994.56					15.70	0.05	15.58	0.03	15.31	0.08	C60
7996.58					15.76	0.05	15.60	0.03	15.33	0.06	C60
7997.25					15.68	0.08	15.55	0.05			M20
8004.58			16.37	0.04	15.89	0.02	15.71	0.03	15.39	0.04	C60
8005.56			16.52	0.04	15.92	0.02	15.75	0.03	15.44	0.04	C60
8006.56			16.52	0.04	15.97	0.02	15.76	0.03	15.46	0.05	C60
8007.57			16.59	0.03	16.00	0.02	15.82	0.02	15.50	0.04	C60
8008.57			16.62	0.05	15.99	0.02	15.83	0.04	15.49	0.05	C60
8009.56			16.63	0.04	16.06	0.03	15.87	0.03	15.55	0.04	C60
8036.60							16.46	0.06	16.09	0.04	L60
8041.64			17.69	0.05	16.98	0.06	16.70	0.04	16.32	0.04	L60
8051.64			17.58	0.05	16.90	0.03	16.70	0.04	16.26	0.04	L60
8074.44					19.02	0.09	18.79	0.06	18.06	0.08	C60

Table 2.: Continued.

JD–	U	σ_U	B	σ_B	V	σ_V	R	σ_R	I	σ_I	Tel.
2450000											
8075.53					19.05	0.05	18.70	0.05	18.07	0.04	C60
8125.40					19.08	0.06	19.02	0.09	18.36	0.09	S100
8145.62			19.73	0.09	18.95	0.04	18.72	0.05	17.91	0.05	K250
8209.40					20.73	0.12	20.91	0.21	19.82	0.09	K250

Table 3. $UBVRI$ magnitudes of local standard stars for AT 2018cow

Star	U	σ_U	B	σ_B	V	σ_V	R	σ_R	I	σ_I
1	14.85	0.07	13.57	0.02	12.47	0.02	11.80	0.02	11.23	0.02
2	15.31	0.05	15.19	0.02	14.52	0.02	14.12	0.02	13.74	0.02
3	17.82	0.06	16.97	0.05	15.86	0.03	15.18	0.03	14.58	0.03
4	16.88	0.06	16.19	0.04	15.15	0.03	14.50	0.03	13.96	0.03
5	16.87	0.06	16.73	0.04	16.06	0.04	15.66	0.03	15.27	0.04
6	16.14	0.05	15.86	0.03	15.17	0.03	14.74	0.03	14.35	0.03

3. SN 2017egm

The light curves of SN 2017egm are presented in Fig. 3, we show our data, the results from Bose et al. (2018), Hosseinzadeh et al. (2021) and Gaia⁵. We plotted the B, V magnitudes from Bose et al. (2018) and transformed their gri magnitudes to the RI bands. The gri magnitudes from Hosseinzadeh et al. (2021) were transformed to the VRI magnitudes. The results by Bose et al. (2018), Hosseinzadeh et al. (2021) are in good agreement with our data, taking into account that transformation relations for normal stars may not work well for SNe.

The light curves clearly show that SN 2017egm belongs to the class of slowly-declining SLSN-I (Inserra et al., 2017). The peculiar feature of SN 2017egm was the linear rise of brightness before maximum, with the rate of $0.068 \text{ mag day}^{-1}$ in all optical bands. The dates of maximum light and maximum magnitudes for the $BVRI$ bands are reported in Table 5. The upper limits of brightness presented by Bose et al. (2018) allows to estimate the explosion epoch at $\text{JD } 2457890 \pm 3$, so the rise to maximum lasted about 36 days, which is quite typical for SLSNe-I.

After a sharp maximum the brightness declined slowly until $\text{JD } 2457963$ (phase about 37 days past maximum), when the rate of decline increased. The

⁵<http://gsaweb.ast.cam.ac.uk/alerts/alert/Gaia17biu/>

Table 4. *UBVRI* photometry of AT2018cow

JD– 2458000	<i>U</i>	σ_U	<i>B</i>	σ_B	<i>V</i>	σ_V	<i>R</i>	σ_R	<i>I</i>	σ_I	Tel.
291.33			14.95	0.04	14.87	0.03	14.85	0.03	14.91	0.04	M70
291.34	13.97	0.07	15.03	0.03	14.94	0.04	14.93	0.04	14.96	0.03	C60
291.39			15.09	0.04	14.94	0.05	14.93	0.03	14.98	0.04	S60
293.31			15.37	0.15							S100
293.46							15.08	0.04			S60
294.33	14.63	0.05	15.65	0.03	15.63	0.04	15.62	0.04	15.44	0.03	C60
295.29	15.07	0.14	15.88	0.04	15.94	0.04	15.81	0.03	15.69	0.04	C60
295.29			15.85	0.04	15.84	0.05	15.78	0.05	15.62	0.04	S100
296.32			16.05	0.04	16.08	0.04	16.02	0.03	15.88	0.04	S100
296.34			16.06	0.04	16.04	0.05	15.96	0.05	15.84	0.07	M70
296.36			16.07	0.04	16.09	0.04	16.03	0.03	15.88	0.05	L60
297.30	15.10	0.08	16.18	0.03	16.26	0.04	16.17	0.03	15.98	0.03	C60
297.33			16.16	0.04	16.16	0.04	16.15	0.06	15.93	0.06	S100
298.32	15.10	0.12	16.32	0.04	16.32	0.03	16.25	0.03	16.08	0.03	C60
299.30	15.31	0.09	16.33	0.04	16.41	0.03	16.36	0.03	16.20	0.03	C60
299.30			16.32	0.05	16.35	0.04	16.25	0.05	16.12	0.08	S100
299.45	15.25	0.05	16.32	0.11	16.44	0.05	16.39	0.04	16.14	0.12	S60
301.31			16.55	0.05	16.64	0.06	16.54	0.07	16.32	0.09	S100
301.33	15.52	0.06	16.66	0.03	16.71	0.03	16.66	0.03	16.45	0.03	C60
301.40	15.38	0.09	16.49	0.06	16.78	0.05	16.96	0.06	16.68	0.13	S60
301.45			16.69	0.05	16.69	0.04	16.62	0.04			L60
302.28			16.72	0.06	16.84	0.07	16.84	0.07	16.46	0.07	S100
303.31	15.89	0.11	16.98	0.04	17.10	0.04	17.07	0.03	16.78	0.04	C60
305.34	16.16	0.09	17.15	0.04	17.21	0.03	17.12	0.03	16.85	0.04	C60
306.29	16.23	0.09	17.20	0.05	17.27	0.04	17.15	0.04	16.90	0.04	C60
308.40			17.41	0.12	17.32	0.15	17.61	0.08	17.18	0.05	S100
309.30	16.43	0.11	17.56	0.04	17.62	0.04	17.52	0.04	17.21	0.04	C60
310.31			17.73	0.06	17.82	0.04	17.79	0.04	17.44	0.04	C60
310.32			17.70	0.04	17.74	0.04	17.69	0.03	17.36	0.03	K250
311.31	17.02	0.11	17.90	0.04	17.97	0.04	17.86	0.03	17.48	0.03	C60
313.37			18.20	0.05	18.26	0.07	18.10	0.08	17.79	0.06	C60
317.28			18.60	0.07	18.68	0.06	18.43	0.07			C60
321.33			19.05	0.06	19.19	0.05	19.00	0.08	18.80	0.08	C60
338.30			20.30	0.04	20.58	0.04	20.17	0.03	19.83	0.04	K250
360.21			22.05	0.08	22.08	0.10	21.43	0.08	21.36	0.11	K250

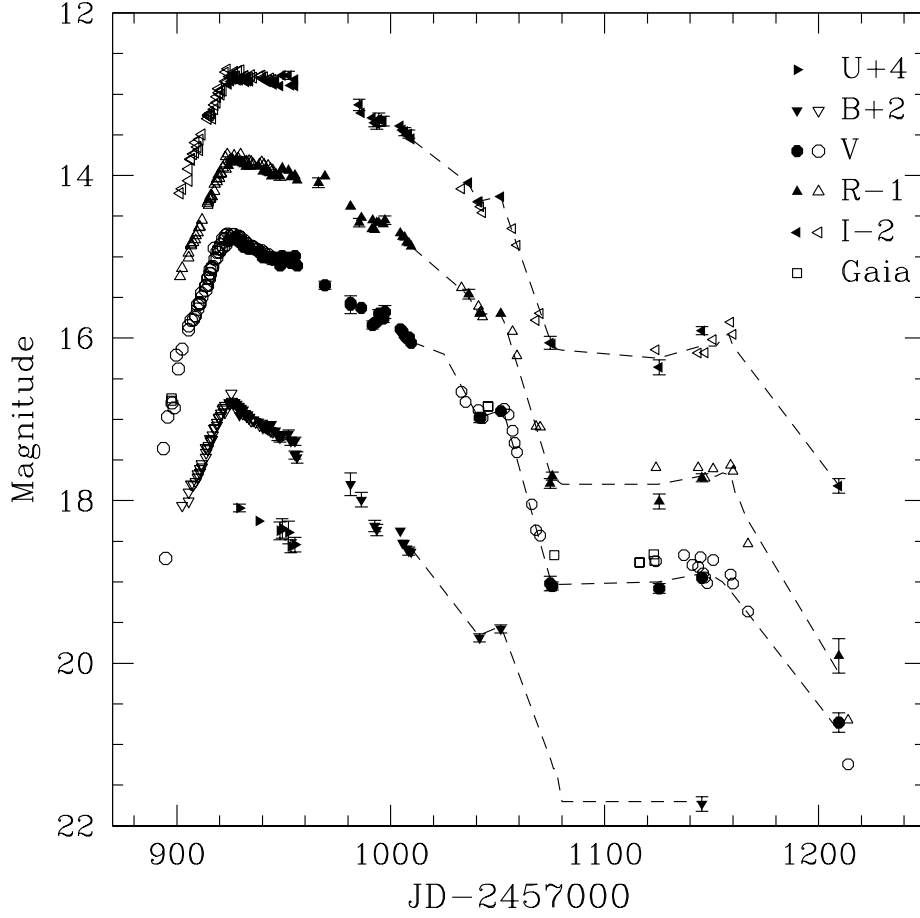


Figure 3. The light curves of SN 2017egm. Filled symbols show our data, and open symbols are for the results from Bose et al. (2018), Hosseinzadeh et al. (2021) and Gaia. The lines connecting points after JD 2458020 are plotted for visual clarity. The error bars are plotted only for out data, when they exceed the size of a symbol.

rates in the phase interval 0-37 days are denoted β_1 in Table 5, while β_2 are the rates from 37 to 100 days past maximum. We should note that β_1 is larger for shorter wavelengths, while β_2 is similar for all optical bands. A bump on the light curve is detected in the period JD 2458040-50. After the bump the decline was faster, at a rate $\sim 0.10 \text{ mag day}^{-1}$. Then we observed the long plateau, which lasted approximately from JD 2458075 until JD 2458160. The existence of these features is confirmed by the data from Hosseinzadeh et al. (2021) and Gaia. After the plateau the rate of decline was quite fast $\sim 0.04 \text{ mag day}^{-1}$.

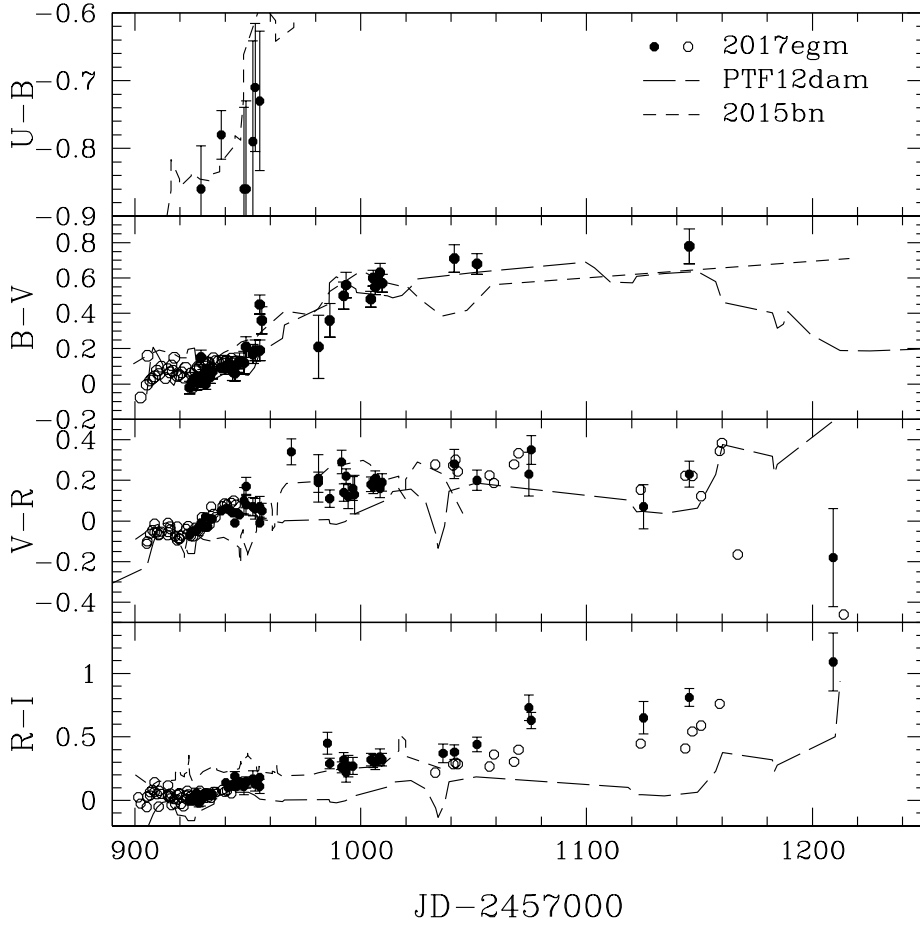


Figure 4. The color curves of SN 2017egm. Filled symbols show our data, and open symbols are for the results from Bose et al. (2018), Hosseinzadeh et al. (2021)

Table 5. Parameters of the light curves of SN 2017egm

	B	V	R	I
$t_{max}, \text{JD-2457000}$	925.1	926.5	927.2	928.1
m_{max}	14.78	14.75	14.81	14.77
$\beta_1, \text{mag day}^{-1}$	0.020	0.012	0.007	0.004
$\beta_2, \text{mag day}^{-1}$	0.020	0.017	0.016	0.015

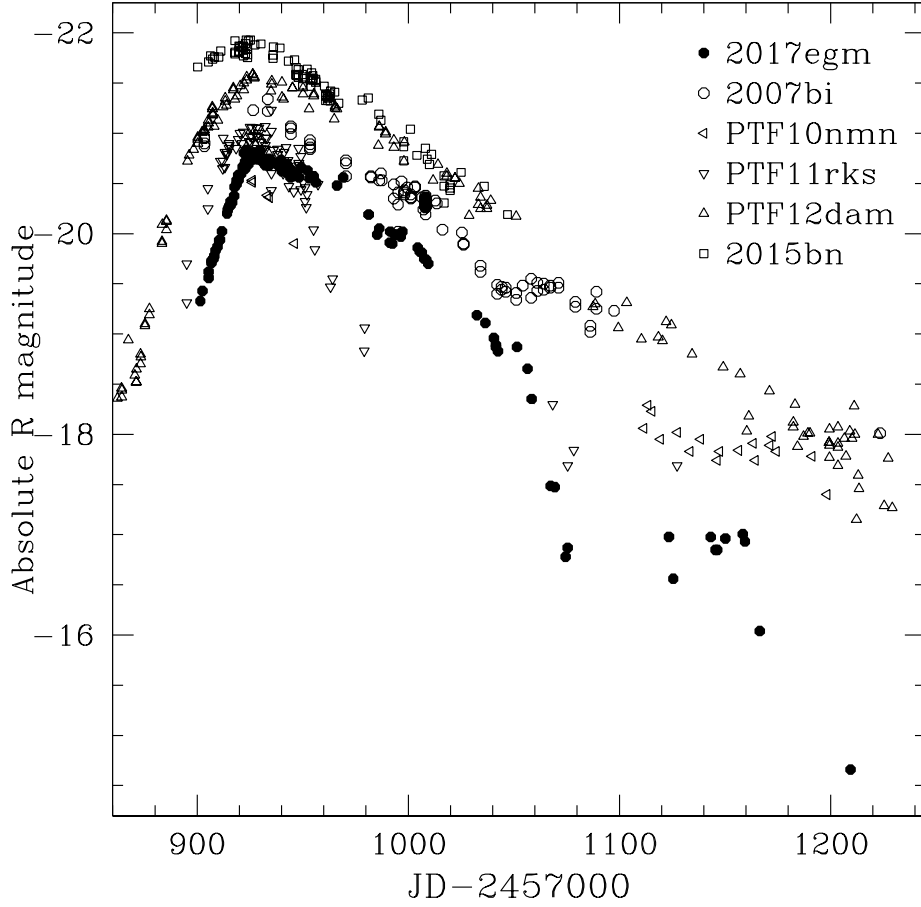


Figure 5. The absolute R -band light curve of SN2017egm compared to the light curves for 5 other SLSNe-I

The color evolution is presented in Fig.4, where the color curves for SLSNe-I PTF12dam (De Cia et al., 2018; Nicholl et al., 2013) and 2015bn (Nicholl et al., 2016) are plotted for comparison. For SN PTF12dam the colors $g - r$ and $r - i$ were transformed to $B - V$, $V - R$ and $R - I$ using relations from Chonis & Gaskell (2008). The color curves show gradual slow reddening from maximum light until the phase ~ 100 days past maximum. After the period of nearly constant colors the color $V - R$ starts decreasing at the phase ~ 200 days, while $R - I$ color continues to increase. The color evolution of two other SLSNe-I is similar, although some difference is observed at late stages, when the colors depend on the variations of emission lines strength.

The absolute R -band light curve of SN2017egm is presented in Fig.5, it is compared to the light curves of SLSNe-I 2007bi, PTF10nmn, PTF11rks,

PTF12dam and 2015bn (Gal-Yam et al., 2009; Young et al., 2010; Nicholl et al., 2013; Inserra et al., 2013; Nicholl et al., 2016; De Cia et al., 2018).

The maximum luminosity of SN 2017egm is within the range for other SLSNe-I. The peculiar feature of SN 2017egm is the linear shape of the light curve before maximum, which is not observed in other objects of this class. The photometric behavior after maximum is similar for SN 2017egm and other SLSNe-I, it is best matched by SN 2007bi. The long plateau at phases 150–230 days is also observed for SN PTF10nmn, although the decline after maximum is faster for this SN. After the plateau the brightness of SN 2017egm declines very fast, and at the epoch ~ 280 days it is significantly fainter than other objects from the comparison sample.

4. AT 2018cow

The light curves are shown in Fig. 6. We plotted our data together with the results of $UBVRI$ photometry from Perley et al. (2019), Margutti et al. (2019) and Xiang et al. (2021). We also show the discovery magnitude and upper limit reported by Smartt et al. (2018), i -band magnitude and upper limit from Fremming (2018) and upper limit in the g band reported by Prentice et al. (2018). The light curves demonstrate very fast rise to the sharp maximum, which occurred on JD 2458287.4. We can estimate maximum magnitudes: $B_{max} = 13.49$; $V_{max} = 13.58$; $R_{max} = 13.71$; $I_{max} = 13.88$, the uncertainties of these magnitudes are about $\sim 0.05 - 0.1$ mag. The decline was nearly linear for the first 10 days after peak, the rates of decline in the BVR bands were nearly equal, at about 0.34 mag day $^{-1}$. The rate was slightly slower in the U band: 0.31 mag day $^{-1}$, and significantly slower in the I band: 0.24 mag day $^{-1}$. The decline started to slow down at the phase ~ 10 days, and 10 days later the decline again becomes nearly linear, with the rates of about 0.08 mag day $^{-1}$ for the $BVRI$ bands and slightly slower 0.07 mag day $^{-1}$ for the U band.

Two bumps can be noticed on the light curves, especially in the U band, at phases ~ 10 and ~ 15 days past maximum. The magnitudes from different sets of data agrees well at the early stages, but for epochs later than ~ 30 days they show large scatter and some systematic differences.

The color evolution is presented in Fig. 7. The characteristic feature of AT 2018cow is the blue color, especially $U - B$, and slow color evolution. Only the $V - R$ color shows gradual reddening, which is the typical color evolution for supernovae.

Assuming the distance to AT 2018cow $D=66.3$ Mpc and Galactic extinction $E(B - V) = 0.08$ mag (Prentice et al., 2018), the absolute magnitudes at maximum are $M_B = -20.95$; $M_V = -20.78$; $M_R = -20.6$; $M_I = -20.37$ mag. Such high luminosity makes AT 2018cow close to SLSNe, although the light curves of SLSNe are generally much broader.

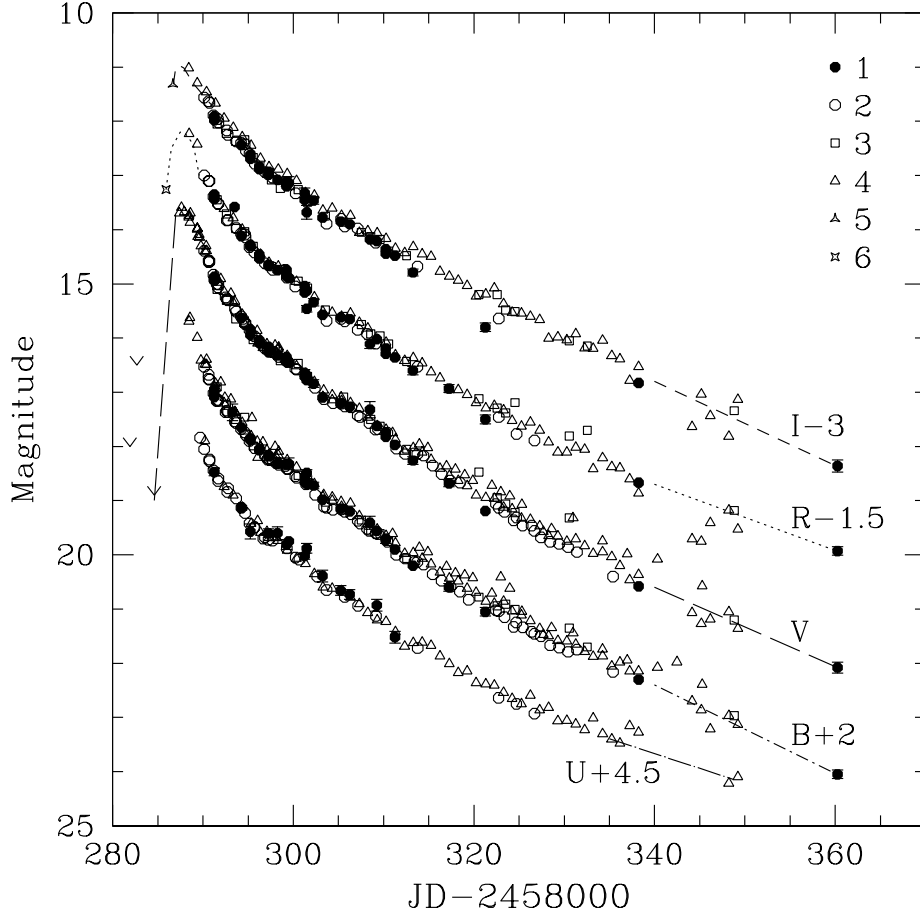


Figure 6. The *UBVRI* light curves of AT 2018cow. Symbols coding: 1: out data, 2: Perley et al. (2019), 3: Margutti et al. (2019), 4: Xiang et al. (2021), 5: Fremling (2018), 6: Smartt et al. (2018)

The comparison of the light and color curves of AT 2018cow with those for different classes of SNe and other transients were made by Perley et al. (2019), Xiang et al. (2021). They showed that fast photometric evolution of AT 2018cow is matched by some objects, for example, by a peculiar fast-evolving transient KSN2015K and SN Ibn LSQ13ccw. The nearly constant blue color was observed for SN Ibn 2006jc. But the maximum luminosity of these objects was significantly lower than that of AT 2018cow.

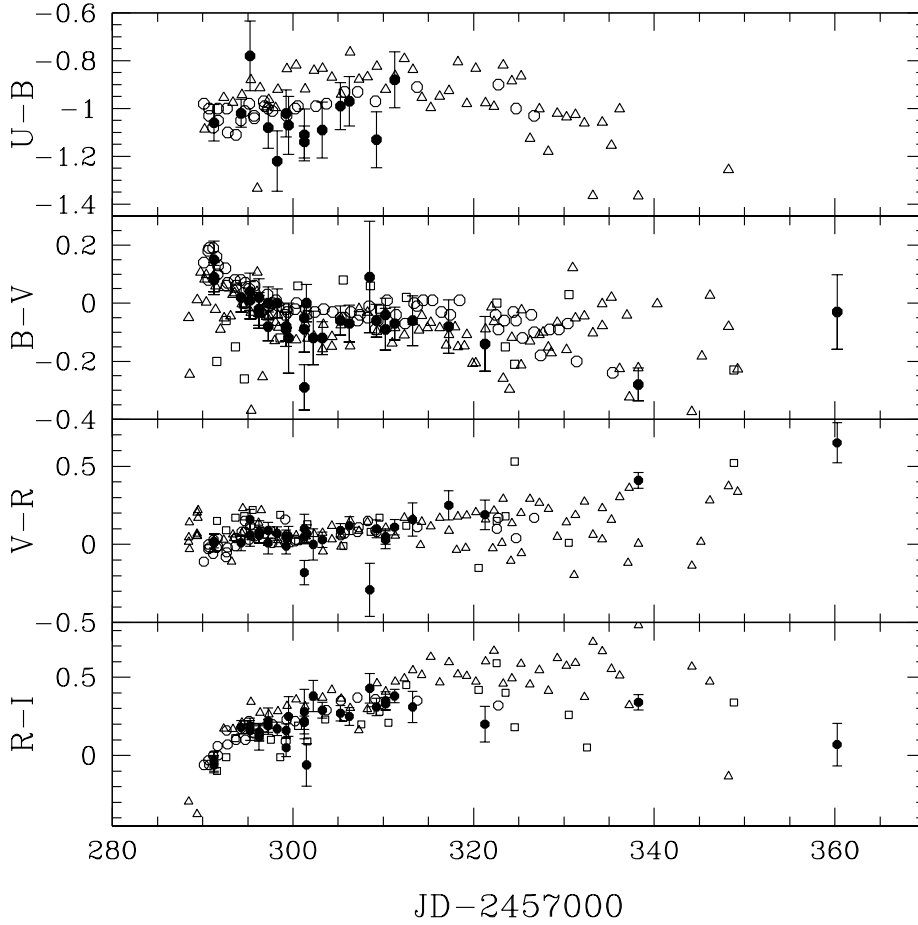


Figure 7. The color curves of AT 2018cow. The symbols are the same as in Fig. 6

5. Conclusions

We presented our photometric observations of type I superluminous supernova SN 2017egm and the peculiar transient AT 2018cow.

The multi-band photometry covered about 285 days of evolution for SN 2017egm. We determined the maximum magnitudes in different bands and the rates of decline for various stages of photometric evolution. The undulations on the light curves were definitely detected: a bump at phase 114 days past maximum and a plateau for phase interval from 155 to 235 days. Our photometric data are in good agreement with the results by Bose et al. (2018) and

Hosseinzadeh et al. (2021). The comparison of light curves and color evolution of SN 2017egm with several objects of similar class revealed that the maximum luminosity and post-maximum evolution of brightness and color of SN 2017egm was not significantly different from those for such well-studied objects, as SLSNe 2007bi, 2015bn and PTF12dam. The peculiar feature of SN 2017egm was the linear part of the light curves before maximum. The undulations on the light curves can be regarded as evidence for interaction of ejecta with the circumstellar material.

Our observations of AT 2018cow continued for about 70 days. They are in good agreement with the data from Perley et al. (2019), Margutti et al. (2019), and Xiang et al. (2021). Our last points in the *BVRI* bands were obtained later than the data from these authors, they are useful for the determination of luminosity evolution at late stage. The main features of the light curves of AT 2018cow are the very short rise time of ~ 2 -3 days, very fast decline after maximum with a rate of about $0.34 \text{ mag day}^{-1}$. The undulations on the light curves were detected. The color evolution is characterized by nearly constant blue colors for the whole period of observations. Some of the features of photometric evolution can be also found for such objects as a peculiar fast-evolving transient KSN2015K and SNe Ibn LSQ13ccw, 2006jc. It is possible that AT 2018cow represents an extreme case of type Ibn SN and the explosion mechanism is the core collapse of a high mass star in a dense shell of circumstellar material (Xiang et al., 2021; Pellegrino et al., 2021).

Acknowledgement

SS is thankful to the the Slovak Academy VEGA 2/0030/21, APVV-20-0148 and M.V.Lomonosov Moscow State University Program "Leading scientific schools", the project "Physics of stars, relativistic objects and galaxies" for the supported of this research.

References

- Benetti, S., Pastorello, A., Cappellaro, E., et al., NUTS update on the spectroscopic follow-up of SN 2018cow. 2018, *The Astronomer's Telegram*, **11836**, 1
- Bietenholz, M. F., Margutti, R., Coppejans, D., et al., AT 2018cow VLBI: no long-lived relativistic outflow. 2020, *Monthly Notices of the RAS*, **491**, 4735, DOI: 10.1093/mnras/stz3249
- Bose, S., Dong, S., Pastorello, A., et al., Gaia17biu/SN 2017egm in NGC 3191: The Closest Hydrogen-poor Superluminous Supernova to Date Is in a "Normal," Massive, Metal-rich Spiral Galaxy. 2018, *Astrophysical Journal*, **853**, 57, DOI: 10.3847/1538-4357/aaa298

- Chonis, T. S. & Gaskell, C. M., Setting UBVRI Photometric Zero-Points Using Sloan Digital Sky Survey ugriz Magnitudes. 2008, *Astronomical Journal*, **135**, 264, DOI: 10.1088/0004-6256/135/1/264
- De Cia, A., Gal-Yam, A., Rubin, A., et al., Light Curves of Hydrogen-poor Superluminous Supernovae from the Palomar Transient Factory. 2018, *Astrophysical Journal*, **860**, 100, DOI: 10.3847/1538-4357/aab9b6
- Dong, S., Bose, S., Chen, P., et al., Re-classification of Gaia17biu/SN 2017egm: the closest hydrogen-poor superluminous supernova yet found, located in a massive host galaxy. 2017, *The Astronomer's Telegram*, **10498**, 1
- Fremling, C., Palomar 48-inch observations of the optical transient AT2018cow/ATLAS18qqn. 2018, *The Astronomer's Telegram*, **11738**, 1
- Gal-Yam, A., The Most Luminous Supernovae. 2019, *Annual Review of Astronomy and Astrophysics*, **57**, 305, DOI: 10.1146/annurev-astro-081817-051819
- Gal-Yam, A., Mazzali, P., Ofek, E. O., et al., Supernova 2007bi as a pair-instability explosion. 2009, *Nature*, **462**, 624, DOI: 10.1038/nature08579
- Hosseinzadeh, G., Berger, E., Metzger, B. D., et al., Bumpy Declining Light Curves are Common in Hydrogen-poor Superluminous Supernovae. 2021, *arXiv e-prints*, arXiv:2109.09743
- Inserra, C., Nicholl, M., Chen, T. W., et al., Complexity in the light curves and spectra of slow-evolving superluminous supernovae. 2017, *Monthly Notices of the RAS*, **468**, 4642, DOI: 10.1093/mnras/stx834
- Inserra, C., Smartt, S. J., Jerkstrand, A., et al., Super-luminous Type Ic Supernovae: Catching a Magnetar by the Tail. 2013, *Astrophysical Journal*, **770**, 128, DOI: 10.1088/0004-637X/770/2/128
- Izzo, L., Thöne, C. C., García-Benito, R., et al., The host of the Type I SLSN 2017egm. A young, sub-solar metallicity environment in a massive spiral galaxy. 2018, *Astronomy and Astrophysics*, **610**, A11, DOI: 10.1051/0004-6361/201731766
- Kuin, N. P. M., Wu, K., Oates, S., et al., Swift spectra of AT2018cow: a white dwarf tidal disruption event? 2019, *Monthly Notices of the RAS*, **487**, 2505, DOI: 10.1093/mnras/stz053
- Leung, S.-C., Blinnikov, S., Nomoto, K., et al., A Model for the Fast Blue Optical Transient AT2018cow: Circumstellar Interaction of a Pulsational Pair-instability Supernova. 2020, *Astrophysical Journal*, **903**, 66, DOI: 10.3847/1538-4357/abba33
- Lyman, J. D., Galbany, L., Sánchez, S. F., et al., Studying the environment of AT 2018cow with MUSE. 2020, *Monthly Notices of the RAS*, **495**, 992, DOI: 10.1093/mnras/staa1243

- Margutti, R., Metzger, B. D., Chornock, R., et al., An Embedded X-Ray Source Shines through the Aspherical AT 2018cow: Revealing the Inner Workings of the Most Luminous Fast-evolving Optical Transients. 2019, *Astrophysical Journal*, **872**, 18, DOI: 10.3847/1538-4357/aafa01
- Maund, J. R., Steele, I., Jermak, H., Wheeler, J. C., & Wiersema, K., RINGO3 polarimetry of the Type I superluminous SN 2017egm. 2019, *Monthly Notices of the RAS*, **482**, 4057, DOI: 10.1093/mnras/sty2963
- Michałowski, M. J., Kamphuis, P., Hjorth, J., et al., Nature of the unusual transient AT 2018cow from HI observations of its host galaxy. 2019, *Astronomy and Astrophysics*, **627**, A106, DOI: 10.1051/0004-6361/201935372
- Nayana, A. J. & Chandra, P., uGMRT Observations of a Fast and Blue Optical Transient—AT 2018cow. 2021, *Astrophysical Journal, Letters*, **912**, L9, DOI: 10.3847/2041-8213/abed55
- Nicholl, M., Berger, E., Margutti, R., et al., The Superluminous Supernova SN 2017egm in the Nearby Galaxy NGC 3191: A Metal-rich Environment Can Support a Typical SLSN Evolution. 2017, *Astrophysical Journal, Letters*, **845**, L8, DOI: 10.3847/2041-8213/aa82b1
- Nicholl, M., Berger, E., Smartt, S. J., et al., SN 2015BN: A Detailed Multi-wavelength View of a Nearby Superluminous Supernova. 2016, *Astrophysical Journal*, **826**, 39, DOI: 10.3847/0004-637X/826/1/39
- Nicholl, M., Smartt, S. J., Jerkstrand, A., et al., Slowly fading super-luminous supernovae that are not pair-instability explosions. 2013, *Nature*, **502**, 346, DOI: 10.1038/nature12569
- Nikolenko, I. V., Kryuchkov, S. V., Barabanov, S. I., & Volkov, I. M., Telescopes of the INASAN Simeiz Observatory: current state and prospects. 2019, *INASAN Science Reports*, **4**, 85, DOI: 10.26087/INASAN.2019.4.2.015
- Pellegrino, C., Howell, D. A., Vinkó, J., et al., Circumstellar Interaction Powers the Light Curves of Luminous Rapidly-evolving Optical Transients. 2021, *arXiv e-prints*, arXiv:2110.15370
- Perley, D. A., Mazzali, P. A., Yan, L., et al., The fast, luminous ultraviolet transient AT2018cow: extreme supernova, or disruption of a star by an intermediate-mass black hole? 2019, *Monthly Notices of the RAS*, **484**, 1031, DOI: 10.1093/mnras/sty3420
- Potantin, S. A., Gorbunov, I. A., Dodin, A. V., et al., Analysis of the optics of the 2.5-m telescope of the Sternberg Astronomical Institute. 2017, *Astronomy Reports*, **61**, 715, DOI: 10.1134/S106377291707006X
- Prentice, S. J., Maguire, K., Smartt, S. J., et al., The Cow: Discovery of a Luminous, Hot, and Rapidly Evolving Transient. 2018, *Astrophysical Journal, Letters*, **865**, L3, DOI: 10.3847/2041-8213/aadd90

- Quimby, R. M., Kulkarni, S. R., Kasliwal, M. M., et al., Hydrogen-poor superluminous stellar explosions. 2011, *Nature*, **474**, 487, DOI: 10.1038/nature10095
- Rivera Sandoval, L. E., Maccarone, T. J., Corsi, A., et al., X-ray Swift observations of SN 2018cow. 2018, *Monthly Notices of the RAS*, **480**, L146, DOI: 10.1093/mnrasl/sly145
- Roychowdhury, S., Arabsalmani, M., & Kanekar, N., H I 21 cm mapping of the host galaxy of AT2018cow: a fast-evolving luminous transient within a ring of high column density gas. 2019, *Monthly Notices of the RAS*, **485**, L93, DOI: 10.1093/mnrasl/slz035
- Saito, S., Tanaka, M., Moriya, T. J., et al., Late-phase Spectropolarimetric Observations of Superluminous Supernova SN 2017egm to Probe the Geometry of the Inner Ejecta. 2020, *Astrophysical Journal*, **894**, 154, DOI: 10.3847/1538-4357/ab873b
- Smartt, S. J., Clark, P., Smith, K. W., et al., ATLAS18qqn (AT2018cow) - a bright transient spatially coincident with CGCG 137-068 (60 Mpc). 2018, *The Astronomer's Telegram*, **11727**, 1
- Soker, N. & Gilkis, A., Explaining iPTF14hls as a common-envelope jets supernova. 2018, *Monthly Notices of the RAS*, **475**, 1198, DOI: 10.1093/mnras/stx3287
- Tsvetkov, D. Y., Pavlyuk, N. N., Shugarov, S. Y., & Volkov, I. M., Optical observations of bright supernovae. 2019, *Contributions of the Astronomical Observatory Skalnaté Pleso*, **49**, 183
- Wheeler, J. C., Chatzopoulos, E., Vinkó, J., & Tuminello, R., Circumstellar Interaction Models for the Bolometric Light Curve of Type I Superluminous SN 2017egm. 2017, *Astrophysical Journal, Letters*, **851**, L14, DOI: 10.3847/2041-8213/aa9d84
- Xiang, D., Song, H., Wang, X., et al., Spectroscopic Classification of SN 2017egm as a Luminous Type II Supernova. 2017, *The Astronomer's Telegram*, **10442**, 1
- Xiang, D., Wang, X., Lin, W., et al., The Peculiar Transient AT2018cow: A Possible Origin of a Type Ibn/IIn Supernova. 2021, *Astrophysical Journal*, **910**, 42, DOI: 10.3847/1538-4357/abdeba
- Yamanaka, M., Nakaoka, T., Kawabata, M., et al., Kanata Optical and Near-infrared Observations of AT 2018cow. 2018, *The Astronomer's Telegram*, **11868**, 1
- Young, D. R., Smartt, S. J., Valenti, S., et al., Two type Ic supernovae in low-metallicity, dwarf galaxies: diversity of explosions. 2010, *Astronomy and Astrophysics*, **512**, A70, DOI: 10.1051/0004-6361/200913004

EDITORIAL

During 2021, the journal Contributions of the Astronomical Observatory Skalnaté Pleso (CAOSP) published 22 articles on 264 pages, and composed of three issues.

Volume 51/1 features the third, final part of the review articles on beta Lyrae and five contributions from the GATE summer school devoted to GAIA and TESS missions, which was held online in Brno, August 8–15, 2020.

Volume 51/2 comprises five regular papers devoted to stellar astrophysics. An interesting result is the finding that the X-ray source 2SXPS J173508.4-292958 is an accreting white dwarf in a symbiotic binary. New fundamental parameters of the eclipsing binary V355 And and its distance were determined in the subsequent paper, while the third paper reports on a new dwarf nova of SU UMa-type ZTF18abdlzhd that was revealed using the Zwicky Transient Facility Data R3. The fourth article presents an interesting finding that a peculiar ER UMa-type dwarf nova, MASTER OT J172758.09+380021.5, is currently in a post-nova state, and underwent a nova eruption relatively recently – hundreds of years ago. The final article reveals the apsidal motion of the eclipsing binary V2783 Ori with the period of ~ 656 years and the presence of a third body in the system with the orbital period of 10 ± 2 years.

Volume 51/3 entails ten selected contributions presented at the “VII Bredikhin conference”, held in Zavolzhsk, Russia, May 24–28, 2021. The Proceeding of the conference were edited by Mikhail Sachkov and Anna Kartashova.

Finally, we also introduced a few small technical changes and amendments. Effective from volume 52 the page numbering scheme was changed, affecting the ADS Bibcode as well. The use of ORCID IDs was slightly modified, which now appear also in PDF versions of papers. All these changes are incorporated in the new version (3.09) of the CAOSP L^AT_EX style, which can be downloaded from the CAOSP website.

Tatranská Lomnica, January 3, 2022

Augustín Skopal, Editor-in-Chief

Richard Komžík, Managing Editor

PRÁCE ASTRONOMICKÉHO OBSERVATÓRIA
NA SKALNATOM PLESE
LII, číslo 1

Zostavovateľ:	RNDr. Richard Komžík, CSc.
Vedecký redaktor:	RNDr. Augustín Skopal, DrSc.
Vydal:	Astronomický ústav SAV, Tatranská Lomnica
IČO vydavateľa:	00 166 529
Periodicita:	3-krát ročne
ISSN (on-line verzia):	1336-0337
CODEN:	CAOPF8
Rok vydania:	2022
Počet strán:	66

Contributions of the Astronomical Observatory Skalnaté Pleso are processed using
L^AT_EX 2_ε CAOSP DocumentClass file 3.09 ver. 2021.